Composite Structures 387 (2026) 120350

Contents lists available at ScienceDirect

Composite Structures

journal homepage: www.elsevier.com/locate/compstruct

A memory-dependent stochastic framework for photoacoustic interactions in poro-semiconductor media under extended Green–Naghdi and spatiotemporal nonlocal effects

Abhik Sur [a], Marin Marin [b,c], Argha Nath Bhattacharyya [d], Murat Yaylacı [e], Soumik Das [f,*]

[a] Department of Mathematics, Sister Nivedita University, West Bengal, India
[b] Department of Mathematics and Computer Science, Transilvania University of Brasov, 500036 Brasov, Romania
[c] Academy of Romanian Scientists, Ilfov Street, 3, 050045 Bucharest, Romania
[d] Department of Statistics, Sister Nivedita University, West Bengal, India
[e] Department of Civil Engineering, Recep Tayyip Erdogan University, 53100, Rize, Turkey
[f] School of Physical Sciences, Amrita Vishwa Vidyapeetham, Mysuru Campus, Karnataka, India

ARTICLE INFO

Keywords:
White noise fluctuations
Wiener process
Photo-thermoelasticity
Modified Green–Naghdi models
Semiconductor
Porosity

ABSTRACT

This study presents a stochastic framework for analyzing coupled photoacoustic thermo-hydro-mechanical interactions in a porous semiconductor medium, extending beyond conventional deterministic models by explicitly incorporating randomness, memory effects, and spatiotemporal nonlocality. Unlike classical approaches that assume idealized and noise-free conditions, the proposed formulation integrates stochastic boundary excitation through a Wiener process, enabling a more realistic representation of laser-induced thermal fluctuations. The constitutive relations are modeled using a Klein–Gordon-type nonlocal operator, incorporating intrinsic length- and time-scale parameters, while heat conduction is described within an extended Modified Green–Naghdi (MGN) framework that accounts for finite-speed propagation. Closed-form analytical solutions are obtained using normal-mode analysis, and numerical simulations are performed for poro-silicon to evaluate the impact of stochasticity on thermophysical fields. The results reveal that stochastic effects significantly amplify the near-surface thermal response, where the variance of temperature, $V_\theta(x,z,t)$, is observed to be approximately 70%–100% higher than the corresponding deterministic solution, indicating that stochasticity can nearly double the effective thermal fluctuations at the boundary. This discrepancy gradually diminishes with increasing depth, leading to convergence between stochastic and deterministic profiles. Additionally, acoustic pressure exhibits pronounced boundary-layer fluctuations before stabilizing within the medium. These findings demonstrate that incorporating stochastic effects is essential for accurately capturing boundary-dominated photoacoustic phenomena in semiconductor materials. The proposed model provides a unified and physically consistent framework that enhances predictive capability and is applicable to advanced technologies such as MEMS devices, photothermal imaging, laser-based material processing, and nanoscale semiconductor systems.

1. Introduction

Mathematical modeling plays a central role in advancing research across physics, mechanics, and microelectronics, particularly in the analysis of coupled multiphysics systems. Traditionally, many such models are formulated within a deterministic framework, which assumes idealized conditions and neglects inherent uncertainties. However, real-world systems are inevitably influenced by stochastic fluctuations arising from environmental disturbances, material heterogeneity, and measurement errors. As a result, deterministic models often fail to fully capture the variability observed in practical scenarios. Incorporating stochastic effects into mathematical formulations provides a more realistic and reliable description of physical processes, thereby enhancing predictive capability and robustness. Several factors [1,2] necessitate this transition: real systems are rarely isolated and are continuously subjected to environmental noise; mathematical models often omit subtle or complex physical mechanisms; and experimental

---

[*] Corresponding author.
E-mail address: soumikdas1993@gmail.com (S. Das).

https://doi.org/10.1016/j.compstruct.2026.120350
Received 4 February 2026; Received in revised form 26 March 2026; Accepted 13 April 2026
Available online 18 April 2026

List of symbols

$\lambda,\ \mu$	Lamé constants
α_s	coefficient of thermal expansion semiconductor
$\gamma = (3\lambda + 2\mu)\alpha_s$	volumetric thermal expansion of semiconductor
ρ_s	density of the semiconductor
ρ_w	pore water density
ρ	density
K	thermal conductivity
D_E	carrier diffusion coefficient
d_n	coefficient of electronic deformation
τ_1	lifetime
E_g	energy gap
m	volumetric heat capacity of the semiconductor
τ_0	relaxation time
α_w	thermal expansion coefficient of pore water
g	gravitational field
k_d	coefficient of permeability
C_s	heat capacity of semiconductor
C_w	heat capacity of pore water
T	temperature field
P	excess pore water pressure
N	carrier density
c_s	sound-sped of the semiconductor
β	volumetric thermal expansion coefficient
∂	adiabatic index
ℓ	intrinsic length-scale
τ	intrinsic time-scale
$\mathcal{T}_0$	reference temperature

observations invariably contain uncertainties. These considerations highlight the importance of stochastic approaches for developing physically consistent and practically relevant models.

The need for stochastic modeling becomes particularly significant in thermal stress analysis of high-temperature systems and advanced materials. In applications such as microelectronic devices, laser-based systems, and heat-resistant structures, uncertainties may arise due to fluctuations in heat-transfer coefficients, variations in external temperature, and unpredictable operating conditions. In practice, accurately characterizing thermal loads and mechanical responses remains a challenging task [3]. For example, spatial and temporal variations in heat-transfer coefficients around stationary gas-turbine blades [4], as well as high-frequency random thermal oscillations in fast breeder reactors [5], introduce considerable complexity into the system behavior. These uncertainties necessitate stochastic formulations to realistically evaluate temperature distributions and associated thermal stresses.

In parallel, the modeling of heat conduction in modern materials requires going beyond the classical Fourier law, which assumes instantaneous propagation of thermal disturbances. This assumption becomes invalid in microscale and nanoscale systems, as well as under ultrafast thermal loading conditions. To address this limitation, non-Fourier thermoelastic theories have been developed, among which the Green–Naghdi (GN) models represent a significant advancement. The GN theories (Types I-III) introduce the concept of thermal displacement, enabling the description of wave-like heat propagation with finite speed. However, these models remain limited in their ability to capture relaxation dynamics, dispersion effects, and memory-dependent behavior observed in real materials.

To overcome these limitations, the Modified Green–Naghdi (MGN) model has been proposed as a generalized framework for thermoelastic analysis. This model incorporates higher-order temporal derivatives of heat flux, multiple relaxation mechanisms, and memory kernels, drawing analogies with viscoelastic models such as Burgers and Kelvin–Voigt types [6,7]. In this context, the parameter τ represents the thermal relaxation time, characterizing the delay in heat flux response and ensuring finite-speed thermal wave propagation. The parameter ℓ denotes the spatial nonlocal length scale, which accounts for long-range interactions within the material and becomes particularly important at micro and nanoscale dimensions. The parameter χ characterizes the strength of memory effects or internal damping, governing the extent to which past thermal states influence the present response. Together, these parameters enable the MGN model to provide a unified description of both diffusive and wave-like heat transport, while capturing nonlocality and memory effects in a physically meaningful manner. Notably, classical theories such as Fourier, Cattaneo–Vernotte, and Lord–Shulman models emerge as limiting cases of this generalized framework. The effectiveness of such non-Fourier formulations in thermoelastic problems has been demonstrated in various studies, including those by Marin and co-workers [8–10].

The Modified Green–Naghdi (MGN) model finds significant application in the analysis of photothermal processes in semiconductor materials, particularly in the study and optimization of laser-based heating and photoacoustic device performance. In semiconductor systems, heat transfer occurs over microscale and nanoscale domains characterized by complex microstructures, carrier–phonon interactions, and strong coupling between thermal, electronic, and elastic fields. Under rapid or localized excitation conditions—such as laser irradiation, ultrafast pulsed heating, or nanoparticle-assisted photothermal enhancement. The classical Fourier heat conduction model becomes inadequate, as it assumes instantaneous thermal propagation [11,12].

In addition to nonlocal and non-Fourier effects, semiconductor materials, especially porous semiconductors such as poro-silicon (PSi) that exhibit strong coupling between thermal, mechanical, electronic, and fluidic fields. These materials are widely used in optoelectronic devices, sensors, and energy systems due to their unique microstructure and multifunctional properties. In such media, temperature gradients induce stress waves that interact with carrier transport and pore-fluid motion, leading to complex thermo-hydro-mechanical coupling. The porous structure further amplifies these interactions by introducing additional degrees of freedom associated with pore pressure and fluid flow.

Such considerations are essential, as real-world semiconductor devices routinely encounter fluctuations arising from laser excitation, environmental variations, and quantum-scale phenomena [13,14]. A rigorous understanding of these coupled wave dynamics has significant implications for MEMS design, laser-assisted material processing, photothermal spectroscopy, and advanced sensing technologies [15,16]. When such systems are subjected to laser irradiation or photothermal excitation, the boundary conditions themselves become uncertain due to fluctuations in energy deposition, surface conditions, and environmental influences. This motivates the incorporation of stochastic boundary conditions into the modeling framework. The combination of stochasticity with nonlocal thermoelasticity is therefore not arbitrary; rather, it reflects the intrinsic physical nature of photothermal semiconductor systems, where uncertainty, microscale effects, and multiphysics coupling coexist.

Motivated by these considerations, the present study focuses on the stochastic analysis of photo-thermoelastic wave propagation in a porous semiconductor half-space. The half-space configuration is particularly relevant for modeling surface-dominated processes such as laser heating, where strong gradients and boundary effects play a dominant role. The proposed formulation integrates stochastic boundary excitation with a spatiotemporal nonlocal model of Klein–Gordon type, enabling a self-consistent description of coupled thermal, mechanical, electronic, hydromechanical, and acoustic fields.

The proposed framework addresses key shortcomings of earlier deterministic approaches by incorporating stochasticity directly into the boundary conditions [17]. Despite this advancement, the model remains subject to assumptions of linear material response and Gaussian white-noise excitation, which may not fully capture the highly nonlinear and multiscale interactions that arise in semiconductors under extreme operating conditions. The principal strengths of the model lie in its enhanced representation of carrier transport in porous semiconductor media, its improved predictive capability for device behavior under laser-induced thermal loading, and its ability to describe wave propagation in environments characterized by uncertainty [18–21]. In contrast to earlier formulations, the present constitutive relations simultaneously account for thermal effects, pore-fluid dynamics, and carrier density variations. By extending the classical Fourier heat conduction law within the modified Green–Naghdi theoretical framework, the governing thermal equation incorporates both thermoelastic coupling and stochastic photoexcitation applied at the boundary. The illuminated surface is subjected to a prescribed laser-generated heat flux, assumed to be traction-free and insulated from photoacoustic and pore-pressure influences. Closed-form analytical solutions to the coupled governing equations are derived using normal-mode analysis. Numerical investigations for poro-silicon (PSi) reveal that stochastic effects significantly modify the near-surface response of the system. Although the discrepancy between stochastic and deterministic solutions decreases with increasing depth, the variance of the stochastic temperature field remains nearly twice that predicted by the deterministic model. Similarly, acoustic pressure exhibits pronounced fluctuations near the boundary before asymptotically converging to the deterministic profile. These results underscore the importance of stochastic modeling for achieving accurate and reliable predictions of photoacoustic phenomena in semiconductor materials. To provide a comprehensive overview of the computational workflow and ensure the reproducibility of the numerical results, the systematic steps involved in solving the coupled poro-photothermoelastic equations through the proposed numerical framework are summarized in Table 1.

2. Extended frameworks for heat propagation models

Drawing inspiration from the conceptual symmetry between viscoelastic mechanics and thermal transport, we introduce the concepts of thermal-viscous and thermal-elastic components. These serve as thermal counterparts to the traditional mechanical dashpot and spring, respectively. We let χ represent the thermal displacement, where its temporal derivative relates to temperature as $\dot{\chi} = T$ [22], and $v = \nabla\chi$ signifies the gradient of this displacement. The governing constitutive relations for these fundamental units are defined as [22]:

$$q = -k^{\star} v, \quad q = -k\dot{v}, \tag{1}$$

In this context, q denotes the heat flux vector, k is the coefficient of thermal conductivity, τ is the relaxation time, and $k^{\star}$ is defined by the ratio k/τ. By leveraging the structural analogy between generalized heat transport and viscoelasticity [22], we can derive advanced constitutive relations. These models are constructed by arranging thermal-elastic and thermal-viscous units in various series and parallel architectures, as depicted in Fig. 1. This framework allows for the derivation of several refined heat conduction models.

2.1. Cattaneo–Vernotte (CV) and Green–Naghdi (GN) variants

(i) The CV-type Formulation

In the CV-based approach, the thermal-elastic and thermal-viscous components are coupled such that a uniform heat flux passes through both elements:

$$q = q_1 = q_2. \tag{2}$$

Table 1

Algorithmic workflow of the proposed stochastic nonlocal model.

Step	Stage	Description
1	Problem Definition	Define geometry, fields, and laser-induced interaction.
2	Constitutive Modeling	Apply nonlocal Klein–Gordon relations with ℓ and τ.
3	Heat Model	Adopt MGN framework with unified parameters χ_i.
4	Governing Equations	Form coupled thermo-hydro-mechanical system.
5	Nondimensionalization	Introduce dimensionless variables.
6	Potential Functions	Use Helmholtz decomposition.
7	Normal Modes	Assume harmonic wave solution.
8	Field Solutions	Obtain analytical expressions.
9	Boundary Conditions	Apply thermal, mechanical, and carrier constraints.
10	Constants Evaluation	Solve algebraic system for coefficients.
11	Stochastic Modeling	Introduce Wiener-based boundary noise.
12	Statistical Measures	Compute mean and variance.
13	Numerical Study	Evaluate using poro-silicon parameters.
14	Visualization	Plot field distributions.
15	Interpretation	Analyze stochastic and nonlocal effects.

The cumulative thermal displacement gradient of the system is obtained by summing the contributions of each individual unit:

$$v = v_1 + v_2, \tag{3}$$

where the individual fluxes are governed by:

$$q_1 = -k^{\star} v_1, \quad q_2 = -k\dot{v}_2. \tag{4}$$

These conditions collectively establish the standard CV heat conduction model.

(ii) The GN-type Transport Model

Conversely, the GN model is characterized by a parallel arrangement of elastic and viscous units. In this configuration, the total heat flux is the sum of the components' fluxes, while the displacement gradient remains identical across units:

$$q = q_1 + q_2, \quad v = v_1 = v_2, \tag{5}$$

with the respective flux laws defined as:

$$q_1 = -k\dot{v}_1, \quad q_2 = -k^{\star} v_2. \tag{6}$$

By integrating Eqs. (5) and (6), the GN model is expressed as:

$$\tau_0 \dot{q} = -k\nabla T - k\tau_0 \nabla\dot{T}. \tag{7}$$

2.2. Modified Green–Naghdi (MGN) architectures

(i) The MGN-I Variant

The MGN-I model is established by placing a thermoelastic element in series with a parallel GN structure, resulting in [23]:

$$\begin{gathered} q = q_1 + q_2, \quad v = v_1 + v_2, \\ \tau_1 \dot{q}_1 = -k_1 \nabla T - k_1 \tau_1 \nabla \dot{T}_1, \quad q_2 = -k_2^{\star} \nabla T_2. \end{gathered} \tag{8}$$

This assembly leads to the generalized relation:

$$\left(\tau_1 + \frac{k_1}{k_2}\tau_2\right)\dot{q} + \frac{k_1}{k_2}\tau_1\tau_2\ddot{q} = -k_1\nabla T - k_1\tau_1\nabla\dot{T}. \tag{9}$$

Assuming standardized parameters for all elements, the expression simplifies to:

$$2\tau_0\dot{q} + \tau_0^2\ddot{q} = -k\nabla T - k\tau_0\nabla\dot{T}. \tag{10}$$

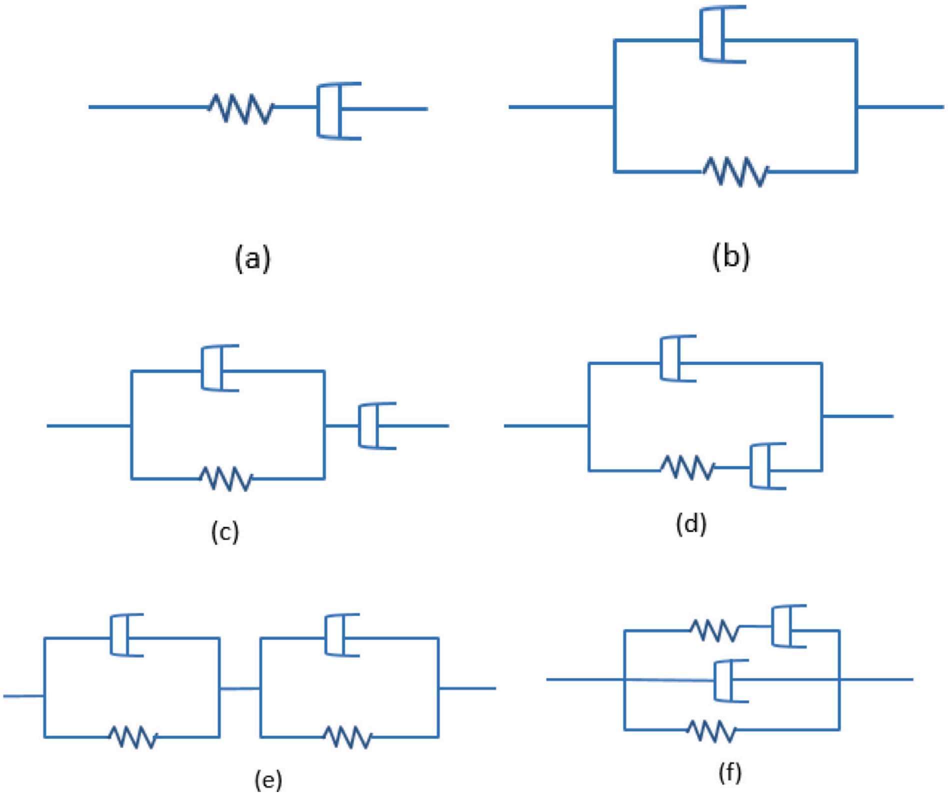

Fig. 1. Representation of generalized modified heat transport models.

(ii) The MGN-II Variant

This model is realized by adding a thermoelastic unit in parallel to a CV-type configuration. The representative equations are [23]:

$$\begin{aligned} &q = q_1 + q_2, \quad \nu = \nu_1 = \nu_2, \\ &q_1 = -k_1^{\star} \nu_1, \quad q_2 + \tau_2 \dot{q}_2 = -k_2 \nabla T_2. \end{aligned} \tag{11}$$

Combining these yields the higher-order transport equation:

$$\frac{k_2}{k_1}\tau_1 \dot{q} + \frac{k_2}{k_1}\tau_1\tau_2 \ddot{q} = -k_2 \nabla T - k_2 \tau_2 \nabla \dot{T} - \frac{k_2^2 \tau_1}{k_1} \nabla \dot{T}. \tag{12}$$

For uniform properties, this reduces to [23]:

$$\tau_0 \dot{q} + \tau_0^2 \ddot{q} = -k \nabla T - 2k\tau_0 \nabla \dot{T}. \tag{13}$$

(iii) The MGN-III Variant

By connecting two GN units in a series sequence, we obtain the following system [23]:

$$\begin{aligned} &q = q_1 + q_2, \quad \nu = \nu_1 + \nu_2, \\ &\tau_i D q_i = -(k_i \tau_i D^2 + k_i D)\nu_i, \quad i = 1, 2 \quad (D \equiv \partial/\partial t). \end{aligned} \tag{14}$$

Under the assumption of homogeneous unit characteristics, the modified law is [23]:

$$2\tau_0 \dot{q} + 2\tau_0^2 \ddot{q} = -k \nabla T - 2k\tau_0 \nabla \dot{T} - k\tau_0^2 \nabla \ddot{T}. \tag{15}$$

(iv) The MGN-IV Variant

This model is constructed by integrating CV and GN units in a parallel arrangement. The governing relations for each branch are [23]:

$$\begin{aligned} &q = q_1 + q_2, \quad \nu = \nu_1 + \nu_2, \\ &q_1 + \tau_1 \dot{q}_1 = -k_1 \nabla T_1, \quad \tau_2 q_2 = -k_2 \nabla T_2 - k_2 \tau_2 \nabla \dot{T}_2. \end{aligned} \tag{16}$$

With identical parameters, the resulting modified Fourier-type law is [23]:

$$\tau_0 \dot{q} + \tau_0^2 \ddot{q} = -k \nabla T - 3k\tau_0 \nabla \dot{T} - k\tau_0^2 \nabla \ddot{T}. \tag{17}$$

In summary, by mapping viscoelastic principles onto heat conduction, we demonstrate that GN-style models can be interpreted as parallel combinations of thermal-viscous and thermal-elastic units. This perspective facilitates the development of the MGN category of models. The dynamic complexity of the flux response is directly tied to the internal arrangement of these components. While the standard GN model involves first-order derivatives, the MGN variants typically introduce second-order temporal derivatives of the heat flux. This hierarchical approach successfully captures advanced thermal phenomena, such as varying heat transfer rates and evolving temperature gradients, offering a more nuanced simulation of physical thermal transport.

3. Basic equations

Klein–Gordon-type nonlocal theory introduces intrinsic spatial and temporal scales into the constitutive relations, allowing the material response at any point to depend not only on local field values but also on the behavior of its surrounding neighborhood and past states [24–26]. This nonlocal formulation captures microstructural interactions, dispersive effects, and finite-speed propagation—features that are particularly important in heterogeneous and porous semiconductor media. Invoking a stochastic photo-thermo-hydro-mechanical interaction in poro-semiconductors, Klein–Gordon-type nonlocality provides a substantial advantage by offering enhanced stability and regularity in the presence of random fluctuations, modeling uncertainty more realistically, and accurately reflecting the influence of pore-scale heterogeneity on coupled optical, thermal, mechanical, and fluid-driven wave dynamics. As consequence, this methodology delivers a more comprehensive and physically consistent explanation of the dynamics of stochastic multiphysics in advanced semiconductor devices.

Corresponding to this case, the constitutive relationship in the context of spatiotemporal nonlocal yields [27–30]

$$\left(1 - \ell^2 \nabla^2 + \tau^2 \frac{\partial^2}{\partial t^2}\right) \sigma_{ij} = \lambda u_{k,k} \delta_{ij} + \mu(u_{i,j} + u_{j,i}) - (P + \gamma T - \delta_n N)\delta_{ij}. \tag{18}$$

The equation of motion in absence of body force is given by [31]

$$(\lambda+\mu)\nabla(\nabla\cdot u)+\mu\nabla^2 u-\nabla P-\gamma\nabla T-\delta_n\nabla N=\rho\ddot{u}. \tag{19}$$

To establish a clear connection between the thermo-viscoelastic framework representing the extension of heat conduction models, it is important to note that the MGN models are systematically embedded into the present formulation through the set of unified parameters χ_i $(i=0,\ 1,\ 2,\ 3,\ 4)$. The MGN architectures, derived via series and parallel combinations of thermal-elastic and thermal-viscous elements, naturally lead to higher-order temporal derivatives of the heat flux and temperature gradients. These features are directly reflected in the generalized constitutive relation and the resulting heat transport equation through terms involving $\dot{T}$, $\ddot{T}$, $\dot{q}$, and $\ddot{\text{q}}$. By appropriately selecting the values of χ_i, the unified model recovers the classical Cattaneo–Vernotte (CV), Green–Naghdi (GN), and all MGN variants as special cases. Thus, the parameter set χ_i serves as a bridge that translates the underlying thermo-viscoelastic network representation into a continuum-level field equation, while simultaneously enabling the incorporation of additional physical effects such as plasma coupling and nonlocal interactions within a single generalized framework.

Observe a scenario when free electrons in a flexible semiconductor substance are triggered by external light rays, causing to a carrier-free variation density with energy E_g, which denotes the gap of the semiconducting device. The absorbed optical energy causes a variation in deformation and elastic waves. On the other hand, the thermal-elastic-plasma waves will alter the general form of heat equation. It has been shown that the quantity of light energy absorbed is proportional to the amount of electron–hole recombination occurs. Following is a statement of the modified Fourier's law which is appropriate for semiconductor materials experiencing plasma effects. Therefore, the modified Fourier law can be express adjoining some unified parameters as follows

$$-\chi_0 K\nabla T-K\chi_1\tau_0\nabla\dot{T}-\chi_2 K\tau_0^2\nabla\ddot{T}-\int\frac{E_g}{\tau_1}N\,d\mathbf{r}=\left(\chi_3\tau_0+\chi_4\tau_0^2 D_t\right)\dot{q}. \tag{20}$$

Therefore, the heat conduction law is governed by

$$\chi_0 K\nabla^2 T+K\chi_1\tau_0\nabla^2\dot{T}+K\chi_2\tau_0^2\nabla^2\ddot{T}+\frac{E_g}{\tau_1}\dot{N}=\left(\chi_3\tau_0+\chi_4\tau_0^2\frac{\partial}{\partial t}\right)\left[m\ddot{T}+\gamma\mathcal{T}_0\ddot{e}\right]. \tag{21}$$

In the heat transport equation, χ_i $(i=0,\ 1,\ 2,\ 3,\ 4)$ are some unified parameters. In particular

$\chi_0=0,\quad \chi_1=1,\quad \chi_2=0,\quad \chi_3=1,\quad \chi_4=1$ corresponds to C-V model,
$\chi_0=1,\quad \chi_1=1,\quad \chi_2=0,\quad \chi_3=1,\quad \chi_4=0$ corresponds to GN model,
$\chi_0=1,\quad \chi_1=1,\quad \chi_2=0,\quad \chi_3=2,\quad \chi_4=1$ corresponds to MGN-I model,
$\chi_0=1,\quad \chi_1=1,\quad \chi_2=2,\quad \chi_3=1,\quad \chi_4=1$ corresponds to MGN-II model,
$\chi_0=1,\quad \chi_1=1,\quad \chi_2=1,\quad \chi_3=2,\quad \chi_4=2$ corresponds to MGN-III model,
$\chi_0=1,\quad \chi_1=3,\quad \chi_2=1,\quad \chi_3=1,\quad \chi_4=1$ corresponds to MGN-IV model.

Thermal-plasma wave coupling during the photoexcitation process governs the carrier continuity relation, which may be expressed as [32–34]

$$\frac{\partial N}{\partial t}=D_E\nabla^2 N-\frac{N}{\tau_1}+\kappa T. \tag{22}$$

The interaction between thermal and plasma waves in the presence of thermal activation coupling parameter $\kappa=\dfrac{\partial N_0}{\partial T}\dfrac{T}{\tau_1}$ is measured by the absorption optical energy, wherein N_0 is the equilibrium carrier concentration.

For water, the mass conservation equation yields [35]

$$b\left(\alpha_w\frac{\partial T}{\partial t}-\frac{\partial e}{\partial t}\right)-\rho_w\frac{\partial^2 e}{\partial t^2}+\nabla^2 P=0. \tag{23}$$

Here, $m=(1-n_0)\rho_s C_s+n_0\rho_w C_w$ in which n_0 symbolizes porosity and $b=\frac{g\rho_w}{k_d}$. Also, the expression $b\left(\alpha_w\frac{\partial T}{\partial t}-\frac{\partial e}{\partial t}\right)$ describes the dynamic linkage between pore pressure variations and the strain-rate of the solid skeleton. Here, γ is given by $\gamma=(3\lambda+2\mu)\alpha_t$, where α_t is the linear thermal expansion coefficient of the semiconductor, while $\delta_n=(3\lambda+2\mu)d_n$, in which d_n denotes the electronic deformation coefficient. The volumetric strain of the material is defined as $e=\nabla\cdot\vec{u}$.

The acoustic waves emitted by the thermal action of plasma in a semiconducting media are characterized by the photoacoustic pressure, which may be described as [35,36]

$$\nabla^2 P_a(\vec{r},t)-\frac{1}{c_s^2}\frac{\partial^2 P_a(\vec{r},t)}{\partial t^2}-\partial\beta_0\frac{\partial T(\vec{r},t)}{\partial t}=0, \tag{24}$$

where c_s is the speed of sound in the material. Also, β_0 denotes the volumetric thermal expansion coefficient and ∂ is the adiabatic index or specific heat ratio of the material.

4. Problem formulation

Consider the photoacoustic thermo-hydro-mechanical interaction in a semiconductor with the rectangular coordinate system $(x,\ y,\ z)$ with x-axis pointing vertically upward as depicted in Fig. 2. For the simplicity of the problem, the wave propagation is further assumed in $xz-$plane. Therefore, in two-dimensional representation, the displacement vector $\vec{u}=(u,0,w)$ and temperature field T are presumed to be function of spatial coordinates x, z and time t only. Thus, we have:

$$\vec{u}=(u(x,z,t),\ 0,\ w=w(x,z,t)),\quad T=T(x,z,t), \tag{25}$$

where u and w denote the horizontal and vertical displacement components of the semiconductor. The constitutive equations for the present problem, in the context of spatiotemporal nonlocal effects, are given by:

$$\begin{aligned}
&\left(1-\ell^2\nabla^2+\tau^2\frac{\partial^2}{\partial t^2}\right)\sigma_{xx}=\lambda e+2\mu\frac{\partial u}{\partial x}-P-\gamma T-\delta_n N,\\
&\left(1-\ell^2\nabla^2+\tau^2\frac{\partial^2}{\partial t^2}\right)\sigma_{zz}=\lambda e+2\mu\frac{\partial w}{\partial z}-P-\gamma T-\delta_n N,\\
&\left(1-\ell^2\nabla^2+\tau^2\frac{\partial^2}{\partial t^2}\right)\sigma_{xz}=\mu\left(\frac{\partial u}{\partial z}+\frac{\partial w}{\partial x}\right).
\end{aligned} \tag{26}$$

The equation of motion for the present problem can be expressed as

$$(\lambda+\mu)\frac{\partial e}{\partial x}+\mu\left(\frac{\partial^2 u}{\partial x^2}+\frac{\partial^2 u}{\partial z^2}\right)-\frac{\partial P}{\partial x}-\gamma\frac{\partial T}{\partial x}-\delta_n\frac{\partial N}{\partial x}=\rho\left(1-\ell^2\nabla^2+\tau^2\frac{\partial^2}{\partial t^2}\right)\ddot{u}, \tag{27}$$

$$(\lambda+\mu)\frac{\partial e}{\partial z}+\mu\left(\frac{\partial^2 w}{\partial x^2}+\frac{\partial^2 w}{\partial z^2}\right)-\frac{\partial P}{\partial z}-\gamma\frac{\partial T}{\partial z}-\delta_n\frac{\partial N}{\partial z}=\rho\left(1-\ell^2\nabla^2+\tau^2\frac{\partial^2}{\partial t^2}\right)\ddot{w}. \tag{28}$$

Based on the modified Green–Naghdi models, the corresponding heat conduction equation for the problem under consideration is stated as

$$\begin{aligned}
&\chi_0 K\left(\frac{\partial^2 T}{\partial x^2}+\frac{\partial^2 T}{\partial z^2}\right)+K\chi_1\tau_0\left(\frac{\partial^2\dot{T}}{\partial x^2}+\frac{\partial^2\dot{T}}{\partial z^2}\right)+\chi_2 K\tau_0^2\left(\frac{\partial^2\ddot{T}}{\partial x^2}+\frac{\partial^2\ddot{T}}{\partial z^2}\right)\\
&\quad+\frac{E_g}{\tau_1}\dot{N}=\left(\chi_3\tau_0+\chi_4\tau_0^2\frac{\partial}{\partial t}\right)\left[m\ddot{T}+\gamma\mathcal{T}_0\frac{\partial^2}{\partial t^2}\left(\frac{\partial u}{\partial x}+\frac{\partial w}{\partial z}\right)\right],
\end{aligned} \tag{29}$$

Invoking suitable nondimensional quantities

$$x^*=c_0\eta x,\quad u^*=c_0\eta u,\quad z^*=c_0\eta z,\quad w^*=c_0\eta z,\quad \ell^*=c_0\eta\ell,\quad t^*=c_0^2\eta t,$$

$$\tau_0^*=c_0^2\eta\tau_0,\quad \tau^*=c_0^2\eta\tau,\quad T^*=\frac{\gamma T}{\lambda+2\mu},\quad \sigma_{ij}^*=\frac{\sigma_{ij}}{\mu},\quad P^*=\frac{P}{\lambda+2\mu},$$

$$N^*=\frac{\delta_n N}{\lambda+2\mu},$$

$$\eta=\frac{m}{K},\quad P_a^*=\frac{P_a}{P_0},\quad c_0=\sqrt{\frac{\lambda+2\mu}{\rho}}$$

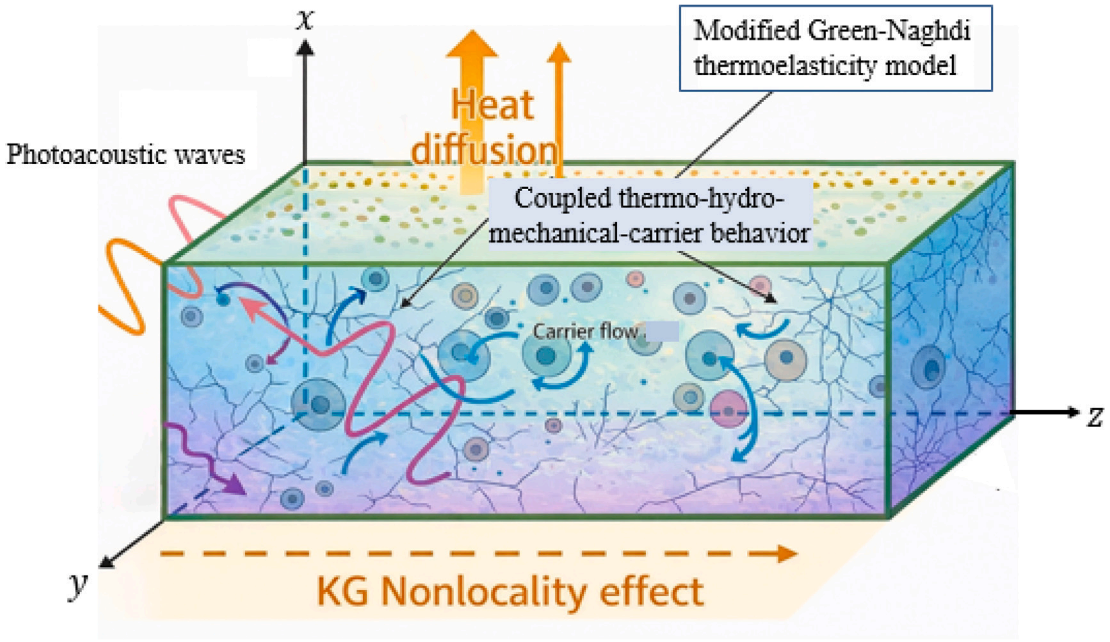

Fig. 2. Geometry of the model.

and after disregarding asterisk, the above equations can be represented in nondimensional form as

$$\left(1-\ell^2\nabla^2+\tau^2\frac{\partial^2}{\partial t^2}\right)\sigma_{xx}=\left(\beta^2-2\right)e+2\frac{\partial u}{\partial x}-\beta^2(P+T+N), \tag{30}$$

$$\left(1-\ell^2\nabla^2+\tau^2\frac{\partial^2}{\partial t^2}\right)\sigma_{zz}=\left(\beta^2-2\right)e+2\frac{\partial w}{\partial z}-\beta^2(P+T+N), \tag{31}$$

$$\left(1-\ell^2\nabla^2+\tau^2\frac{\partial^2}{\partial t^2}\right)\sigma_{xz}=\frac{\partial u}{\partial z}+\frac{\partial w}{\partial x}, \tag{32}$$

$$\left(1-\frac{1}{\beta^2}\right)\frac{\partial e}{\partial x}+\frac{1}{\beta^2}\nabla^2 u-\frac{\partial P}{\partial x}-\frac{\partial T}{\partial x}-\frac{\partial N}{\partial x}=\left(1-\ell^2\nabla^2+\tau^2\frac{\partial^2}{\partial t^2}\right)\ddot{u}, \tag{33}$$

$$\left(1-\frac{1}{\beta^2}\right)\frac{\partial e}{\partial z}+\frac{1}{\beta^2}\nabla^2 w-\frac{\partial P}{\partial z}-\frac{\partial T}{\partial z}-\frac{\partial N}{\partial z}=\left(1-\ell^2\nabla^2+\tau^2\frac{\partial^2}{\partial t^2}\right)\ddot{w}, \tag{34}$$

$$\left(\nabla^2-\epsilon_1\frac{\partial}{\partial t}-\frac{\epsilon_1}{\tau_1}\right)N+\epsilon_2 T=0, \tag{35}$$

$$\begin{aligned}&\chi_0\nabla^2 T+\chi_1\tau_0\nabla^2\dot{T}+\chi_2\tau_0^2\nabla^2\ddot{T}+\epsilon_3\dot{N}\\&\quad=\left(\chi_3\tau_0+\chi_4\tau_0^2\frac{\partial}{\partial t}\right)\left[\ddot{T}+\epsilon_T\frac{\partial^2}{\partial t^2}\left(\frac{\partial u}{\partial x}+\frac{\partial w}{\partial z}\right)\right],\end{aligned} \tag{36}$$

$$\nabla^2 P-\left(\epsilon_5\frac{\partial}{\partial t}+\epsilon_6\frac{\partial^2}{\partial t^2}\right)e+\epsilon_4\frac{\partial T}{\partial t}=0, \tag{37}$$

$$\left(\nabla^2-\epsilon_p\frac{\partial^2}{\partial t^2}\right)P_a-\eta_p\frac{\partial}{\partial t}=0, \tag{38}$$

where

$$\epsilon_1=\frac{1}{D_E\eta},\quad \epsilon_2=\frac{\kappa\delta_n}{D_E c_0^2\eta^2\gamma},\quad \epsilon_3=\frac{E_g\gamma c_0^2\eta}{\tau_1 m\delta_n},\quad \epsilon_T=\frac{\gamma^2\mathcal{T}_0}{m(\lambda+2\mu)},$$

$$\beta^2=\frac{\lambda+2\mu}{\mu},\quad \epsilon_4=\frac{b\alpha_w}{\gamma\eta},\quad \epsilon_5=\frac{b}{\eta(\lambda+2\mu)},\quad \epsilon_6=\frac{\rho_w}{\rho},\quad \epsilon_p=\frac{c_0^2}{c_s^2},$$

$$\eta_p=\partial\beta_0\frac{\rho c_0^2}{\gamma\eta P_0}.$$

By invoking the Helmholtz decomposition theorem, the displacement field is expressed in terms of the potential functions q and $\vec{U}$ as follows:

$$\vec{u}=\nabla q+\nabla\times\vec{U},\quad \nabla\cdot\vec{U}=0. \tag{39}$$

In this formulation, $q(x,z,t)$ and $\vec{U}(x,z,t)$ correspond to the scalar and vector potential functions, respectively. Hence, the displacement components u and w may be written in terms of these potentials by the relations given below:

$$u=\frac{\partial q}{\partial x}+\frac{\partial\psi}{\partial z},\quad w=\frac{\partial q}{\partial z}-\frac{\partial\psi}{\partial x}\quad\text{while}\quad \psi=(-\vec{U})_y, \tag{40}$$

so that, the above equations reduce to

$$\nabla^2 q-\left(1-\ell^2\nabla^2+\tau^2\frac{\partial^2}{\partial t^2}\right)\frac{\partial^2 q}{\partial t^2}-(P+T+N)=0, \tag{41}$$

$$\frac{1}{\beta^2}\nabla^2\psi-\left(1-\ell^2\nabla^2+\tau^2\frac{\partial^2}{\partial t^2}\right)\frac{\partial^2\psi}{\partial t^2}=0. \tag{42}$$

5. Solution of the problem

The physical quantities admit a normal mode representation, which can be written as follows:

$$\begin{aligned}&\left(q,\ \psi,\ P_a,\ T,\ \sigma_{ij},\ N,\ P\right)(x,z,t)\\&\quad=\left(q^\star,\ \psi^\star,\ P_a^\star,\ T^\star,\ \sigma_{ij}^\star,\ N^\star,\ P^\star\right)(x)e^{\omega t+icz},\end{aligned} \tag{43}$$

where ω (complex) is the frequency, c represents the wave number along z–direction whereas $q^\star,\ \psi^\star,\ P_a^\star,\ T^\star,\ \sigma_{ij}^\star,\ N^\star,\ P^\star$ being the amplitudes of the respective thermophysical fields. Recalling the relationship of normal modes defined in the relation (43), thereinafter Eqs. (30)–(42) can be respectively expressed as

$$\left(D^2-\alpha_1\right)N^\star+\epsilon_2 T^\star=0, \tag{44}$$

$$\left[D^2-(c^2+c_{42})\right]T^\star-\epsilon_T c_{42}(D^2-c^2)q^\star+c_{41}N^\star=0, \tag{45}$$

$$(D^2-c^2)P^\star-\left(\epsilon_5\omega+\epsilon_6\omega^2\right)(D^2-c^2)q^\star+\epsilon_4\omega T^\star=0, \tag{46}$$

$$\left(D^2-c^2-\epsilon_p\omega^2\right)P_a^\star=\eta_p\omega T^\star, \tag{47}$$

$$c_{53}D^2\Psi^\star-c_{54}\psi^\star=0, \tag{48}$$

$$c_{52}D^2 q^\star-c_{51}q^\star-(P^\star+T^\star+N^\star)=0, \tag{49}$$

$$\left(\xi_1 - \ell^2 D^2\right) \sigma^{\star}_{xx} = \beta^2 D^2 q^{\star} + 2c^2 q^{\star} + 2ciD\psi^{\star} - \beta^2 (P^{\star} + T^{\star} + N^{\star}), \tag{50}$$

$$\left(\xi_1 - \ell^2 D^2\right) \sigma^{\star}_{zz} = \left(\beta^2 - 2\right) D^2 q^{\star} + \beta^2 c^2 q^{\star} - 2ciD\psi^{\star} - \beta^2 (P^{\star} + T^{\star} + N^{\star}), \tag{51}$$

$$\left(\xi_1 - \ell^2 D^2\right) \sigma^{\star}_{xz} = -D^2 \psi^{\star} + 2icDq^{\star} - c^2 \psi^{\star}, \tag{52}$$

Solving the above set of equations, we arrive at the differential equations satisfied by $N^{\star}$ and $P^{\star}$ as follows

$$\left(D^6 - \mathcal{J}_1 D^4 + \mathcal{J}_2 D^2 - \mathcal{J}_3\right)\left(N^{\star},\ P^{\star}\right) = 0, \tag{53}$$

where

$$\begin{array}{ll}
\alpha_1 = c^2 + \epsilon_1 \omega + \frac{\epsilon_1}{\tau_1}, & c_{41} = \dfrac{\epsilon_3 \omega}{\chi_0 + \chi_1 \tau_0 + \chi_2 \tau_0^2 \omega^2}, \\
c_{42} = \dfrac{\left(\chi_3 \tau_0 + \chi_4 \tau_0^2 \omega\right) \omega^2}{\chi_0 + \chi_1 \tau_0 + \chi_2 \tau_0^2 \omega^2}, & \xi_1 = 1 + \ell^2 c^2 + \tau^2 \omega^2, \\
c_{51} = c^2 + \omega^2 (1 + \ell^2 c^2 + \tau^2 \omega^2), & c_{52} = 1 + \ell^2 \omega^2, \\
c_{53} = 1 + \beta^2 \ell^2 \omega^2, & c_{54} = c^2 - \beta^2 \omega^2 (1 + \ell^2 c^2 + \tau^2 \omega^2), \\
c_{61} = \epsilon_5 \omega + \epsilon_6 \omega^2, & c_{62} = c^2 + \epsilon_p \omega^2, \\
c_{63} = c^2 + c_{42}, & c_{71} = c_{63} + \alpha_1, \\
c_{72} = c_{63} \alpha_1 - c_{41} \epsilon_2, & c_{73} = c_{61} c_{71} + \epsilon_4 \epsilon_T c_{42} \omega, \\
c_{74} = c_{61} c_{72} + \epsilon_4 \epsilon_T c_{42} \omega \alpha_1, & \mathcal{J}_1 = \dfrac{c_{81} - c_{61}}{c_{52}}, \\
\mathcal{J}_2 = \dfrac{c_{82} - c_{73}}{c_{52}}, & \mathcal{J}_3 = \dfrac{c_{83} - c_{74}}{c_{52}}, \\
c_{81} = c_{52} c_{71} + c_{51} + \epsilon_T c_{42}, & c_{82} = c_{52} c_{72} + c_{51} c_{71} + \epsilon_T c_{42} c^2 \\
 & \quad + \epsilon_T c_{42} (\alpha_1 + \epsilon_2), \\
c_{83} = c_{51} c_{72} + \epsilon_T c_{42} c^2 (\alpha_1 + \epsilon_2), & D = \frac{d}{dx}.
\end{array}$$

Eq. (53) further can be expressed as

$$\left(D^2 - k_1^2\right)\left(D^2 - k_2^2\right)\left(D^2 - k_3^2\right)\left(N^{\star},\ P^{\star}\right) = 0, \tag{54}$$

The solution of the differential Eq. (54) is given by

$$N^{\star}(x) = \sum_{i=1}^{3} A_i e^{-k_i x}, \tag{55}$$

$$P^{\star}(x) = \sum_{i=1}^{3} h_{1i} A_i e^{-k_i x}, \tag{56}$$

where

$$h_{1i} = \frac{c_{61} k_i^4 - c_{73} k_i^2 + c_{74}}{\epsilon_2 \epsilon_T c_{42} \left(c^2 - k_i^2\right)}, \quad i = 1,\ 2,\ 3.$$

Therefore, substituting the solution for carrier density and excess pore water pressure from Eqs. (55) and (56) in Eq. (44) yields the temperature distribution as

$$T^{\star}(x) = \sum_{i=1}^{3} h_{2i} A_i e^{-k_i x}, \tag{57}$$

in which,

$$h_{2i} = \frac{\alpha_1 - k_i^2}{\epsilon_2}.$$

Substituting the solutions from Eqs. (55)–(57) in Eq. (49), the solution for the scalar potential function $q(x, z, t)$ yields

$$q^{\star}(x) = \mathcal{B} e^{-k_j x} + \frac{1}{c_{52}} \sum_{i=1}^{3} \frac{\left(h_{1i} + h_{2i} + 1\right)}{k_i^2 - k_j^2} A_i e^{-k_i x}, \tag{58}$$

where $k_j^2 = \frac{c_{51}}{c_{52}}$.

Also, the solution of the potential function Ψ can be obtained from Eq. (48) in the following form

$$\psi^{\star}(x) = \mathcal{C} e^{-k_\eta x}, \tag{59}$$

Also, the solution for the photoacoustic pressure is obtained from differential Eq. (47) in the following form

$$P_a^{\star}(x) = \mathcal{D} e^{-k_\alpha x} + \eta_p \omega \sum_{i=1}^{3} \frac{h_{2i}}{k_i^2 - k_\alpha^2} A_i e^{-k_i x}, \tag{60}$$

in which, $k_\eta^2 = \frac{c_{54}}{c_{53}}$ and $k_\alpha^2 = c_{62}$.

Further, from Eqs. (50) and (52), the amplitudes of the stress distributions have been represented as

$$\sigma^{\star}_{xx}(x) = \frac{\mathcal{B}(\beta^2 k_j^2 + 2c^2)}{\xi_1 - \ell^2 k_j^2} e^{-k_j x} - \frac{2cik_\eta}{\xi_1 - \ell^2 k_\eta^2} \mathcal{C} e^{-k_\eta x} + \sum_{i=1}^{3} \left(\frac{h_{1i} + h_{2i} + 1}{\xi_1 - \ell^2 k_i^2}\right) \left\{ \frac{\left(\beta^2 k_i^2 + 2c^2\right)}{c_{52}\left(k_i^2 - k_j^2\right)} - \beta^2 \right\} A_i e^{-k_i x}, \tag{61}$$

$$\sigma^{\star}_{xz}(x) = -\frac{\mathcal{C}\left(k_\eta^2 + c^2\right)}{\xi_1 - \ell^2 k_\eta^2} e^{-k_\eta x} - 2ic \left[\frac{k_j \mathcal{B}}{\xi_1 - \ell^2 k_j^2} e^{-k_j x} + \frac{1}{c_{52}} \sum_{i=1}^{3} \frac{\left(h_{1i} + h_{2i} + 1\right) k_i}{\left(k_i^2 - k_j^2\right)\left(\xi_1 - \ell^2 k_i^2\right)} A_i e^{-k_i x} \right]. \tag{62}$$

6. Boundary conditions and surface constraints

(i) The surface photoacoustic pressure arises from the synergistic interaction between volumetric strain induced by photoexcited carriers and the thermoelastic expansion resulting from instantaneous laser heating. This coupling creates a transient rise in the local stress field, serving as the primary source for acoustic wave generation. These pressure disturbances then propagate into the bulk medium, effectively dissipating energy as photoacoustic waves [37–40]. Consequently, the acoustic pressure at the boundary interface $x = 0$ is defined as [37–39]:

$$\mathcal{P}_{ac}(0, z, t) = 0. \tag{63}$$

(ii) To account for energy deposition at the irradiated surface, we define a thermal flux boundary condition. This formulation incorporates both the predictable absorption of the laser source and the inherent stochasticity arising from excitation noise [41–43]. Such a stochastic approach provides a high-fidelity representation of photo-thermo-mechanical energy transfer. For a ramp-type thermal excitation, the condition is specified as [38,43]:

$$\left.\frac{\partial T}{\partial x}\right|_{x=0} = \frac{\hat{q}_0}{K} \exp\left(-\frac{\rho^2}{\zeta_G}\right) = \mathcal{T}_0. \tag{64}$$

In this expression, ρ represents the Gaussian radial coordinate of the laser spot, ζ_G denotes the characteristic beamwidth, and $\hat{q}_0$ signifies the maximum heat flux intensity.

(iii) Based on Biot's poroelasticity theory, the pore pressure at the boundary is dictated by fluid flux constraints. In the current configuration [44], the absence of hydraulic permeability between the porous semiconductor and its environment implies that the fluid pressure at the interface vanishes:

$$\mathcal{P}(0, z, t) = 0. \tag{65}$$

(iv) The peripheral plane of the semiconductor is assumed to be isolated from external laser-induced carrier generation or recombination effects. This leads to the following Dirichlet boundary condition for carrier density:

$$N(0, z, t) = \bar{N}, \tag{66}$$

where $\bar{N}$ represents the steady-state equilibrium carrier concentration.

(v) Finally, we assume the semiconductor surface is mechanically traction-free, a condition typical for half-space problems where the material is in contact with air or a vacuum. The resulting normal and tangential stress components at the boundary are:

$$\sigma_{xx}(0,z,t)=0, \tag{67}$$

$$\sigma_{xz}(0,z,t)=0. \tag{68}$$

By applying these boundary constraints to the governing Eqs. (55)–(62), the following system of equations is established:

$$\begin{aligned}
&\mathcal{D}+\eta_p\omega\sum_{i=1}^{3}\frac{h_{2i}}{k_i^2-k_\alpha^2}A_i=0,\\
&\sum_{i=1}^{3}h_{2i}k_iA_ie^{\omega t+icz}=T_0,\\
&\sum_{i=1}^{3}h_{1i}A_i=0,\\
&\sum_{i=1}^{3}A_ie^{\omega t+icz}=N_0,\\
&\frac{\mathcal{B}(\beta^2k_j^2+2c^2)}{\xi_1-\ell^2k_j^2}-\frac{2cik_\eta}{\xi_1-\ell^2k_\eta^2}\mathcal{C}+\sum_{i=1}^{3}\left(\frac{h_{1i}+h_{2i}+1}{\xi_1-\ell^2k_i^2}\right)\left\{\frac{(\beta^2k_i^2+2c^2)}{c_{52}\left(k_i^2-k_j^2\right)}-\beta^2\right\}A_i=0,\\
&\frac{\mathcal{C}\left(k_\eta^2+c^2\right)}{\xi_1-\ell^2k_\eta^2}+2ic\left[\frac{k_j\mathcal{B}}{\xi_1-\ell^2k_j^2}+\frac{1}{c_{52}}\sum_{i=1}^{3}\frac{\left(h_{1i}+h_{2i}+1\right)k_i}{\left(k_i^2-k_j^2\right)\left(\xi_1-\ell^2k_i^2\right)}A_i\right]=0.
\end{aligned} \tag{69}$$

The solution of the algebraic system (69) determines the unknown coefficients A_i ($i=1,\ 2,\ 3$), $\mathcal{B}$, $\mathcal{C}$ and $\mathcal{D}$. Consequently, the solution procedure for the present problem is finalized.

7. Stochastic framework for thermophysical field evolutions

To simulate real-world irregularities within the semiconductor medium — particularly those involving carrier migration and electrical conductivity — we embed stochastic variables into the analytical model. The inherent uncertainty in charge carrier kinetics is modeled by introducing random fluctuations into the governing relations, under the premise of a Gaussian white-noise distribution. This methodology facilitates an exploration of how randomness impacts wave mechanics, while the selected mathematical transformations ensure that the fundamental statistical features of the random processes are preserved.

Incorporating probabilistic elements into the governing equations provides a higher-fidelity understanding of semiconductor material responses under erratic environmental conditions. By integrating Wiener processes, we can effectively simulate random variations in conductivity, carrier concentration, and thermal parameters. These stochastic variables alter energy dissipation patterns and dispersion characteristics by adding uncertainty to the signal propagation pathways.

Under specific regimes, random fluctuations can modify wave stability and damping by broadening the spectral breadth. In contrast to purely deterministic frameworks, the application of Wiener noise necessitates a probabilistic interpretation, relying on variance and expected value analysis to clarify physical phenomena. Additionally, stochastic influences on boundary conditions produce time-varying disturbances that affect thermo-mechanical responses at material interfaces. This refined approach offers a more realistic depiction of semiconductor behavior for nanoelectronics and optoelectronics, where micro-level changes in charge density or temperature profoundly affect global system dynamics.

7.1. Static temperature component

The resolved deterministic temperature field is given by:

$$\mathcal{T}(x,z,t)=\left(\sum_{n=1}^{3}h_{2n}\mathcal{A}_ne^{-\kappa_nx}\right)\exp(\omega t+icz), \tag{70}$$

where the boundary constraint is defined as:

$$\mathcal{T}_1(t)=\mathcal{T}_0(t)=\Theta^\star\mathcal{H}(t)\quad\text{for } t>0, \tag{71}$$

7.2. Randomized thermal distribution

The intrinsic thermal noise at conducting surfaces is represented by a stochastic boundary condition. Such variability may arise from laser power instability, photon flux, or ambient disturbances. For analytical consistency, the boundary thermal input is treated as a white-noise signal, the integral of which yields a Wiener process. While physical thermal noise often possesses a finite correlation (colored noise), the white-noise approximation is the standard convention in semiconductor transport physics for identifying dominant boundary uncertainties. Thus, the thermal boundary is defined via a random process $\rho_0(t)$:

$$\mathcal{T}_0(t)=\mathcal{T}_1+\rho_0(t), \tag{72}$$

where $\rho_0(t)$ is a stochastic function characterized by the zero-expectation property:

$$\mathbb{E}\left[\rho_0(t)\right]=0. \tag{73}$$

Assuming $\rho_0(t)$ behaves as white noise, the following property holds for any non-random signal:

$$\mathbb{E}\left[\mathcal{T}(x,z,t)\right]=\mathcal{T}(x,z,t) \tag{74}$$

The Wiener process $\mathcal{W}_t$ is established by the following criteria:

1. Initialization: $\mathcal{W}_0=0$ almost surely.
2. Independence: For any $t>0$, the future increment $\mathcal{W}_{t+u}-\mathcal{W}_t$ is independent of the past.
3. Gaussian Nature: Increments follow a normal distribution, $\mathcal{W}_{t+u}-\mathcal{W}_t\sim\mathcal{N}(0,u)$.
4. Continuity: The sample paths are continuous with probability one.

Based on these properties, the temperature relation (70) is reorganized as:

$$\mathcal{T}(x,z,t)=\psi(x,z,t)+\Gamma(x,z,t)\mathcal{T}_0 \tag{75}$$

Substituting (72) into (75) results in:

$$\begin{aligned}
\mathcal{T}(x,z,t)&=\psi(x,z,t)+\Gamma(x,z,t)[\mathcal{T}_1+\rho_0(t)]\\
&=\{\psi(x,z,t)+\Gamma(x,z,t)\Theta^\star\}+\Gamma(x,z,t)\rho_0(t)\\
&=\mathcal{T}^{det}(x,z,t)+\Gamma(x,z,t)\rho_0(t),
\end{aligned}$$

where $\mathcal{T}^{det}$ denotes the non-stochastic baseline solution.

Treating white noise $\rho(t)$ as the derivative of the Wiener process ($d\mathcal{W}/dt$), the integral form is:

$$\mathcal{T}(x,z,t)=\mathcal{T}^{det}(x,z,t)+\int_0^t\Gamma(x,z,t-u)\rho(u)du \tag{76}$$

Using the Ito representation:

$$\mathcal{T}(x,z,t)=\mathcal{T}^{det}(x,z,t)+\int_0^t\Gamma(x,z,t-u)d\mathcal{W}(u). \tag{77}$$

The autocorrelation for the thermal process $\mathcal{T}(t)$ is computed as:

$$\begin{aligned}
\mathcal{R}_{\mathcal{T}\mathcal{T}}(t_1,t_2)&=\mathbb{E}[\mathcal{T}(t_1)\mathcal{T}(t_2)]\\
&=\mathbb{E}[\mathcal{T}_1^{det}\mathcal{T}_2^{det}]+\Gamma_1\Gamma_2\mathcal{R}_{\rho_0\rho_0}(t_1,t_2)
\end{aligned}$$

When $t_1=t_2=t$, the mean square value becomes:

$$\mathbb{E}[\mathcal{T}^2(x,z,t)]=\int_0^t(\Gamma(x,z,\xi))^2d\xi+(\mathbb{E}[\mathcal{T}(x,z,t)])^2 \tag{78}$$

Hence, the temperature field variance is defined by:

$$\mathcal{V}ar[\mathcal{T}(x,z,t)]=\int_0^t(\Gamma(x,z,\xi))^2d\xi. \tag{79}$$

7.3. *Carrier concentration fluctuations*

The deterministic carrier density is given by:

$$\mathcal{N}(x,z,t)=\left(\sum_{n=1}^{3}\mathcal{A}_n e^{-\kappa_n x}\right)\exp(\omega t+icz) \tag{80}$$

The expected carrier concentration coincides with the non-stochastic model:

$$\mathbb{E}[\mathcal{N}(x,z,t)]=\mathcal{N}(x,z,t) \tag{81}$$

Applying the same probabilistic integration:

$$\mathcal{N}(x,z,t)=\mathcal{N}^{det}(x,z,t)+\int_0^t \Psi(x,z,t-u)\rho(u)du \tag{82}$$

The variance for the concentration field is:

$$\mathcal{V}ar[\mathcal{N}(x,z,t)]=\int_0^t \Psi^2(x,z,\xi)d\xi \tag{83}$$

7.4. *Pore-water pressure stochasticity*

The baseline pore-water pressure field is defined as:

$$\mathcal{P}(x,z,t)=\left(\sum_{n=1}^{3}h_{1n}\mathcal{A}_n e^{-\kappa_n x}\right)\exp(\omega t+icz) \tag{84}$$

Its mean value is identical to the deterministic solution:

$$\mathbb{E}[\mathcal{P}(x,z,t)]=\mathcal{P}(x,z,t) \tag{85}$$

The total pressure field in the stochastic domain is:

$$\mathcal{P}(x,z,t)=\mathcal{P}^{det}(x,z,t)+\int_0^t \Upsilon(x,z,t-u)\rho(u)du \tag{86}$$

The variance for this field is evaluated as:

$$\mathcal{V}ar[\mathcal{P}(x,z,t)]=\int_0^t \Upsilon^2(x,z,\xi)d\xi. \tag{87}$$

Following this methodology, the stochastic behaviors of displacement and stress distributions can be similarly resolved.

8. Numerical results and interpretations

With an aim to illustrate the solution of the thermophysical quantities such as the temperature, displacement, carrier density, stress, excess pore water pressure and photoacoustic pressure in the space–time domain, we now implement suitable numerical scheme for the determination of the solution. For the purpose of numerical illustration, poro-silicon (Psi) is used due to its spongy and nanostructured form with tiny pores [21], created by etching bulk silicon, giving a huge surface area and unique optical/electrical properties [45,46].

$$\begin{array}{lll}
\lambda = 3.64\times10^{10}\ \mathrm{N\ m^{-2}}, & \mu = 5.46\times10^{10}\ \mathrm{N\ m^{-2}}, & \rho_s = 2.3\times10^{3}\ \mathrm{kg\ m^{-3}}, \\
\rho_w = 10^{3}\ \mathrm{kg\ m^{-3}}, & k_d = 10^{-8}\mathrm{m\ s^{-1}}, & C_w = 4\times10^{3}\ \mathrm{J\ kg^{-1}\ K^{-1}}, \\
\alpha_w = 2\times10^{-4}\ {}^\circ\mathrm{C^{-1}}, & C_s = 6\times10^{2}\ \mathrm{J\ kg^{-1}\ K^{-1}}, & \mathcal{T}_0 = 800\ \mathrm{K}, \\
d_n = -9\times10^{-31}\ \mathrm{m^3}, & D_E = 2,5\times10^{-3}\mathrm{m^2\ s^{-1}}, & E_g = 1.11\ \mathrm{eV}, \\
\alpha_s = 4.14\times10^{-6}\ \mathrm{K^{-1}}, & K = 150\ \mathrm{W\ m^{-1}\ K^{-1}}, & \rho = 2000\ \mathrm{kg\ m^{-3}}, \\
\tau_0 = 0.2, & p = 100\ \mathrm{N}, & N_0 = 9.65\times10^{9}\ \mathrm{cm^{-3}}, \\
\theta_1 = 300\ \mathrm{K}, & c_s = 8430\ \mathrm{m\ s^{-1}}, & \beta_0 = 2.56\times10^{-6}\ {}^\circ\mathrm{C}, \\
\partial = 1.6666, & q_0 = 1.27\times10^{6}\ \mathrm{W\ m^{-2}}, & r = 0.5\times10^{-3}\ \mathrm{m}, \\
\delta_G = 0.354\ \mathrm{m}, & \ell = 0.2, & \tau = 0.1, \\
n_0 = 0.4, & P_0 = 100\ \mathrm{N}, & \tau_1 = 5\times10^{-5}\ \mathrm{s}, \\
\omega = 5+2i, & c = 5, & z = 0.2.
\end{array}$$

8.1. *Implications of nonlocal length scales parameter on deterministic variables*

This subsection illustrates how the thermophysical quantities such as the temperature, carrier density, water pressure, acoustic pressure, normal stress and the shearing stress are influenced by the variation of the intrinsic nonlocal length-scale parameter ℓ. The numerical computations at instant $t = 0.15$ and the characteristic time-scale parameter is assumed as $\tau = 0.10$ for length $z = 0.2$. In these analysis, the heat conduction equation is framed in the context of MGN-IV model.

To evaluate the role of the nonlocal length-scale parameter ℓ on the variation of the temperature against the height x of the photothermal poro-silicon medium, Fig. 3(a) has been depicted. It is seen that the temperature profile attains the maximum magnitude on the plane $x = 0$, and gradually the temperature decreases with the increase of the height of the medium. The behavior is quite plausible since, the plane $x = 0$ is subjected to a prescribed heat flux.

Fig. 3(b) illustrates the variation of carrier density as a function of the height x within the optoelastic medium. The carrier density profile exhibits the peak value at $x = 0$, in accordance with the prescribed boundary conditions. As x increases, the carrier density decreases rapidly near $x = 0.1$, after which the profile shows negligible variation, indicating that the influence of carrier density diminishes beyond this point. This sharp decline suggests that the carrier density is strongly localized near the surface, with minimal penetration into the medium at larger values of x.

Fig. 3(c) illustrates the spatial variation of water pressure along the height of the photothermoelastic medium at a specific time $t = 0.15$. It is observed that the water pressure is nullified at the plane $x = 0$, which is in strict compliance with the mechanical boundary conditions of the system, confirming the validity and correctness of the numerical models and computational procedures used in the analysis. The water pressure distribution exhibits a noticeable decrease within the region $0 < x < 0.25$, beyond which it increases sharply before eventually decaying at a distance further from the plane $x = 0$. This observed behavior is consistent with the expected physical interactions governing the system.

In comparison to the preceding figures, the influence of the nonlocal length scale parameter becomes significantly more prominent in this case. The spatial nonlocal parameter ℓ, which characterizes the scale of nonlocal interactions in the medium, plays a crucial role in modulating the pressure distribution. As ℓ increases, the magnitude of the water pressure profile diminishes, suggesting that the nonlocal effects act to smooth out the pressure gradient. This attenuation in the pressure distribution can be attributed to the fact that the nonlocal interactions effectively “dilute” the localized mechanical effects, thereby reducing the localized pressure peaks. This is a direct consequence of the nonlocality, which introduces a spatial dependence in the material’s response, leading to a more uniform pressure distribution over the domain.

However, one can note that from Fig. 3(d), from the variation of the acoustic pressure P_a, the effect of spatial nonlocality is not reflected.

Fig. 3(e) presents the variation of the normal stress σ_{xx} as a function of the height of the photothermal semiconductor, for the specified set of parameters. At the boundary $x = 0$, the stress distribution conforms to the mechanical boundary conditions, validating the model’s consistency. The stress wave propagates in a characteristic wave-like pattern near this boundary, with the amplitude of the wave diminishing as the height of the medium increases, which suggests attenuation of the stress response with depth. Notably, the spatial nonlocal parameter exhibits a pronounced influence on the stress variation. As this parameter increases, the peak of the stress wave within the poro-silicon medium is significantly enhanced, indicating that nonlocal effects amplify stress concentration, particularly in the near-boundary regions. This behavior underscores the importance of the nonlocal parameter in governing the stress distribution and highlights its potential role in optimizing material design for photothermal applications.

Fig. 3(f) depicts the variation of the shearing stress σ_{xz} for different spatial nonlocal parametric values and the other set of parameters remains invariant as already stated. As revealed from the graphical

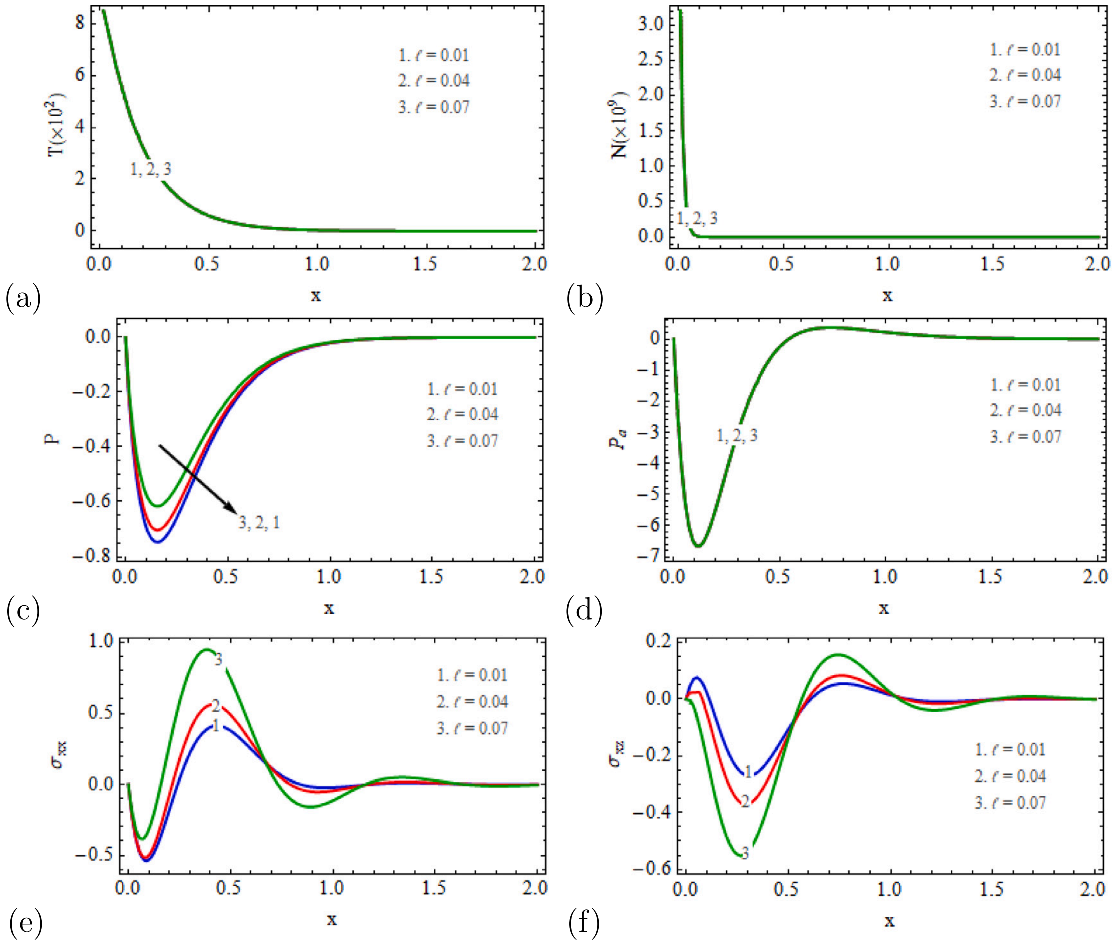

Fig. 3. Two-dimensional contour maps of deterministic variables (a) temperature T, (b) carrier density N, (c) water pressure P, (d) acoustic pressure P_a, (e) normal stress σ_{xx}, and (f) shear stress σ_{xz} for different nonlocal length scale parameter values.

illustration, a similar qualitative behavior can be revealed due to the presence of spatial nonlocality.

8.2. Implications of nonlocal time scales parameter on deterministic variables

This subsection is designed to report the significance of the temporal nonlocal parameter τ while analyzing the variation of the thermophysical quantities which are relevant for analyzing the photothermal effects of the semiconductor. In these analysis, the heat conduction equation is framed in the context of MGN-IV model.

A clear distinction is observed between the roles of spatial and temporal nonlocality in governing the thermophysical responses of the photothermal semiconductor. In the case of spatial nonlocality, an increase in the corresponding nonlocal parameter directly alters the magnitude of the physical fields, reflecting the enhanced influence of long-range spatial interactions within the medium. Conversely, a contrasting behavior is exhibited by temporal nonlocality. As demonstrated in Figs. 4(a), 4(b), and 4(d), variations in the temporal nonlocal parameter τ do not affect the spatial distributions of temperature, carrier density, or acoustic pressure. However, its influence becomes significant in the evolution of water pressure and stress fields, where an increase in τ leads to a systematic reduction in their magnitudes. This attenuation can be attributed to the memory-dependent nature of temporal nonlocality, which effectively distributes the system's response over past states, thereby weakening instantaneous pressure and stress propagation. Hence, while spatial nonlocality amplifies field intensities through extended spatial coupling, temporal nonlocality acts as a dissipative or relaxation-like mechanism, suppressing dynamic mechanical responses within the medium.

8.3. Consequences of various thermoelastic models on deterministic variables

In this subsection, the conventional Green–Naghdi (GN) theory and the generalized MGN-I, MGN-II, MGN-III, and MGN-IV models have been compared to analyze the variation of the thermophysical quantities. For the purpose of illustration, the spatiotemporal nonlocal parameters have been considered as $\ell = 0.01$ and $\tau = 0.01$.

Fig. 5(a) presents the temperature distribution within the photothermal semiconductor as predicted by different modified Green–Naghdi (MGN) thermoelastic models. In comparison with the conventional Green–Naghdi formulation, all MGN models exhibit a markedly sharper decay of temperature, indicating enhanced thermal wave attenuation due to the inclusion of additional relaxation and coupling mechanisms. Among these theories, the MGN-IV model yields the highest temperature magnitude, followed by the MGN-II and MGN-I models, whereas the MGN-III model predicts the lowest temperature response. This variation can be attributed to the distinct ways in which each modified Green–Naghdi theory incorporates thermal relaxation times, non-Fourier heat conduction effects, and thermoelastic coupling. Models with stronger relaxation and coupling effects retain thermal energy over longer spatial extents, leading to higher temperature amplitudes, while those with more pronounced dissipative mechanisms promote

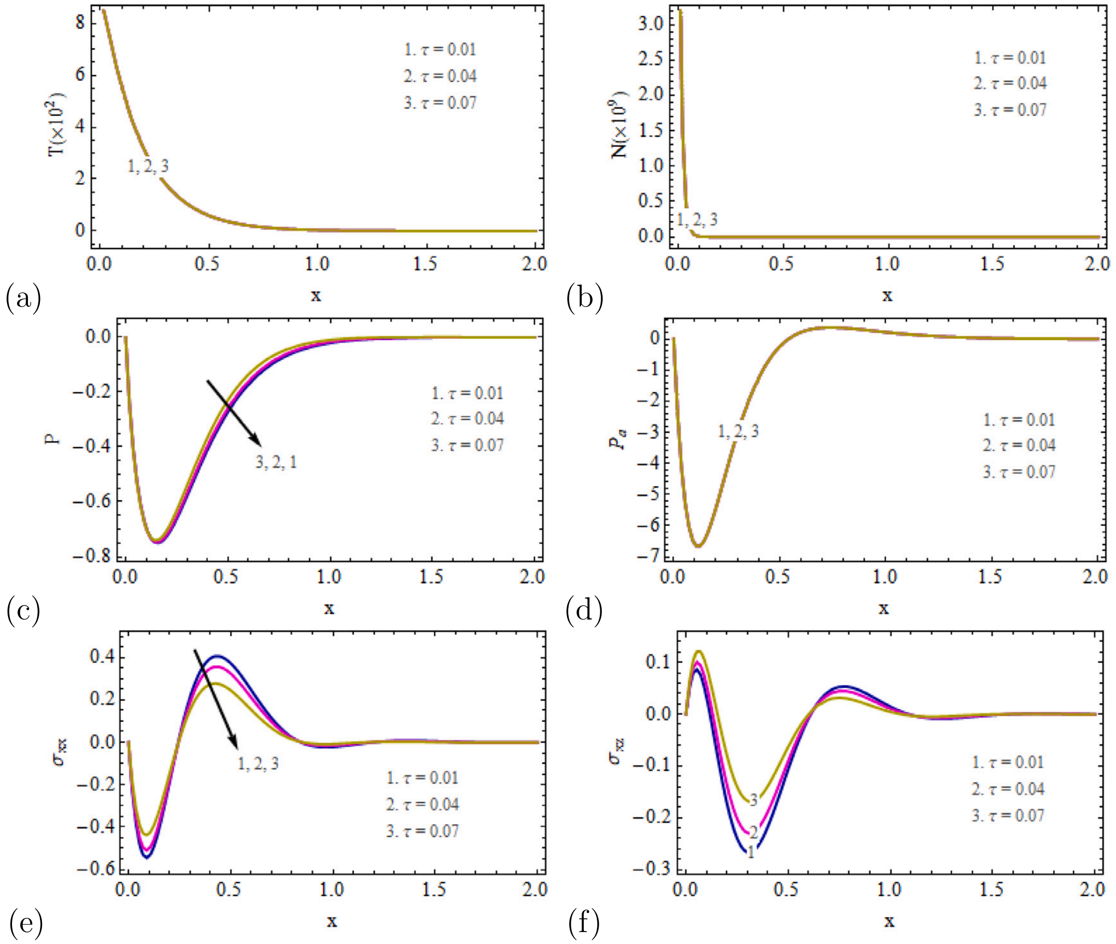

Fig. 4. Two-dimensional contour maps of deterministic variables (a) temperature T, (b) carrier density N, (c) water pressure P, (d) acoustic pressure P_a, (e) normal stress σ_{xx}, and (f) shear stress σ_{xz} for different nonlocal time scale parameter values.

faster thermal decay. Consequently, the observed hierarchy of temperature profiles reflects the intrinsic differences in the thermal wave propagation and energy dissipation characteristics embedded within the respective MGN formulations.

From Fig. 5(b), one can say that the absence of variation in the carrier density distribution among different modified Green–Naghdi (MGN) models can be attributed to the fact that these theories primarily modify the heat conduction mechanism through the introduction of thermal relaxation and non-Fourier effects, without altering the fundamental carrier transport processes. The carrier density evolution is governed mainly by the diffusion–recombination equation and the optical generation term, which remain identical across all MGN formulations. Consequently, the mathematical structure of the carrier density equation remains unchanged, leading to an identical carrier density profile for all modified Green–Naghdi theories considered.

However, Fig. 5(c) reveals a pronounced influence of the underlying thermoelastic formulation on the spatial variation of the water pressure P. In contrast to the temperature and carrier density fields, the water pressure exhibits a strong dependence on the chosen thermoelastic model. The generalized modified Green–Naghdi (MGN) theories predict a substantially higher magnitude of P compared to the conventional Green–Naghdi model, reflecting the enhanced thermo-mechanical coupling and wave-like heat transport incorporated in these formulations. Among the generalized models, the water pressure attains its maximum magnitude for the MGN-II model, followed by the MGN-IV and MGN-III models, while the MGN-I model yields the lowest pressure response. This ordering underscores the sensitivity of fluid-solid interaction and pressure propagation to the specific thermal relaxation and coupling mechanisms embedded within each MGN theory.

As observed from Figs. 5(d)–5(f), the generalized modified Green–Naghdi (MGN) models predict significantly higher magnitudes of acoustic pressure and stress distributions within the semiconductor compared to the conventional Green–Naghdi theory. This enhancement arises from the inclusion of thermal relaxation and non-Fourier heat conduction effects in the generalized MGN formulations, which strengthen thermoelastic coupling and promote wave-like propagation of mechanical disturbances. Consequently, the generalized MGN models capture more pronounced acoustic and stress responses than those predicted by the classical GN framework.

8.4. Distribution of stochastic variables for different sample paths

In the present stochastic framework, this subsection examines the degree of randomness induced in the physical fields due to stochastic boundary conditions, where Gaussian white noise is incorporated through a Wiener process as depicted in Figs. 6(a)–6(f). These computations have been analyzed in the context of MGN-IV model of generalized thermoelasticity in which, the spatiotemporal nonlocal effects have been represented by $\ell = \tau = 0.01$.

The level of randomness is quantitatively characterized by the variance of the stochastic term, which governs the magnitude of fluctuations in temperature, carrier density, pore-water pressure, acoustic pressure, and stress responses. Stronger deviations from deterministic expectations are produced by a larger variance, while responses that closely approximate the deterministic model are produced by

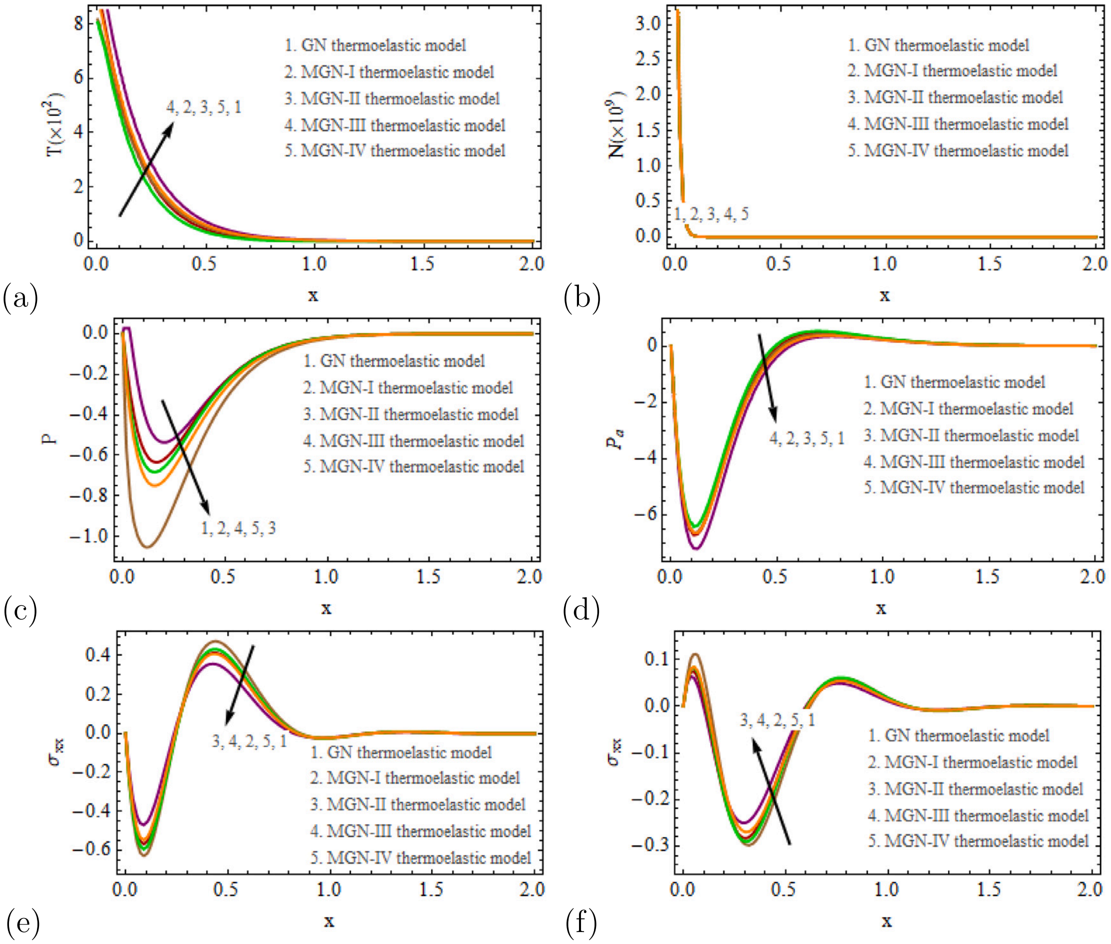

Fig. 5. Two-dimensional contour maps of deterministic variables (a) temperature T, (b) carrier density N, (c) water pressure P, (d) acoustic pressure P_a, (e) normal stress σ_{xx}, and (f) shear stress σ_{xz} for different thermoelasticity theories.

a smaller variance. In terms of Physics, this variation could be the result of uncertainties brought on by variations in laser-heating intensity, carrier-recombination processes, or environmental disturbances which influence semiconducting devices. Three illustrations sample paths corresponding to $t = 0.1,\ 0.2$, and 0.3 are superimposed on the deterministic physical fields in order to capture the stochastic behavior.

Thermal fluctuations being most perceptible on the excitation surface and diminish as thermal waves move inward, in line with the temperature field variance, which achieves its maximum close to the boundary and progressively decreases with increasing depth into the material. The variance profiles of the mechanical stress, acoustic pressure, pore water pressure, and carrier density, on the contrary hand, show an apparent different tendency. The variance for these fields starts at zero at the boundary, grows to a maximum at an intermediate depth, and then settles down to zero. The observed pattern implies that stochastic effects related to fluid transport, mechanical deformation, acoustic wave propagation, and charge carrier creation reach peak instability at particular depths before stabilizing. Under stochastic excitation, these reactions demonstrate the complex interplay of electronic, thermal, mechanical, hydromechanical, and photoacoustic processes in semiconductors.

8.5. *Distribution of variances of stochastic variables*

Figs. 7(a)–7(f) depict the stochastic responses of physical fields subjected to photo-thermoelastic excitation with random boundary perturbations. The incorporation of Gaussian white noise reveals that stochasticity significantly alters wave propagation characteristics compared to deterministic predictions. Temperature profiles display path-dependent wavefront distortions, indicating spatially non-uniform thermal diffusion under random excitation. The carrier density field exhibits amplified fluctuations, emphasizing the role of stochastic transport and recombination processes that cannot be captured by deterministic models alone.

The pore water pressure response shows irregular spatial variations, reflecting random fluid migration governed by strong hydromechanical coupling. Acoustic pressure fluctuations are pronounced near the excitation surface and gradually attenuate with depth, eventually approaching the deterministic state due to dissipative effects. The displacement and stress fields similarly demonstrate stochastic deviations, confirming that mechanical responses are strongly influenced by boundary randomness. Overall, the model reveals an exponential decay of variance in temperature and displacement, while carrier density, pore water pressure, acoustic pressure, and stress exhibit peak-type variance distributions, underscoring the importance of stochastic modeling for realistic semiconductor device analysis.

8.6. *Heat map demonstrating deterministic variables*

In this subsection,Figs. 8(a)–8(f) present the heat maps of the deterministic physical fields in a photothermoelastic semiconductor medium for the spatiotemporal nonlocal parameters $\ell = 0.01$ and $\tau = 0.01$, evaluated within the framework of the modified Green–Naghdi MGN-IV thermoelastic model.

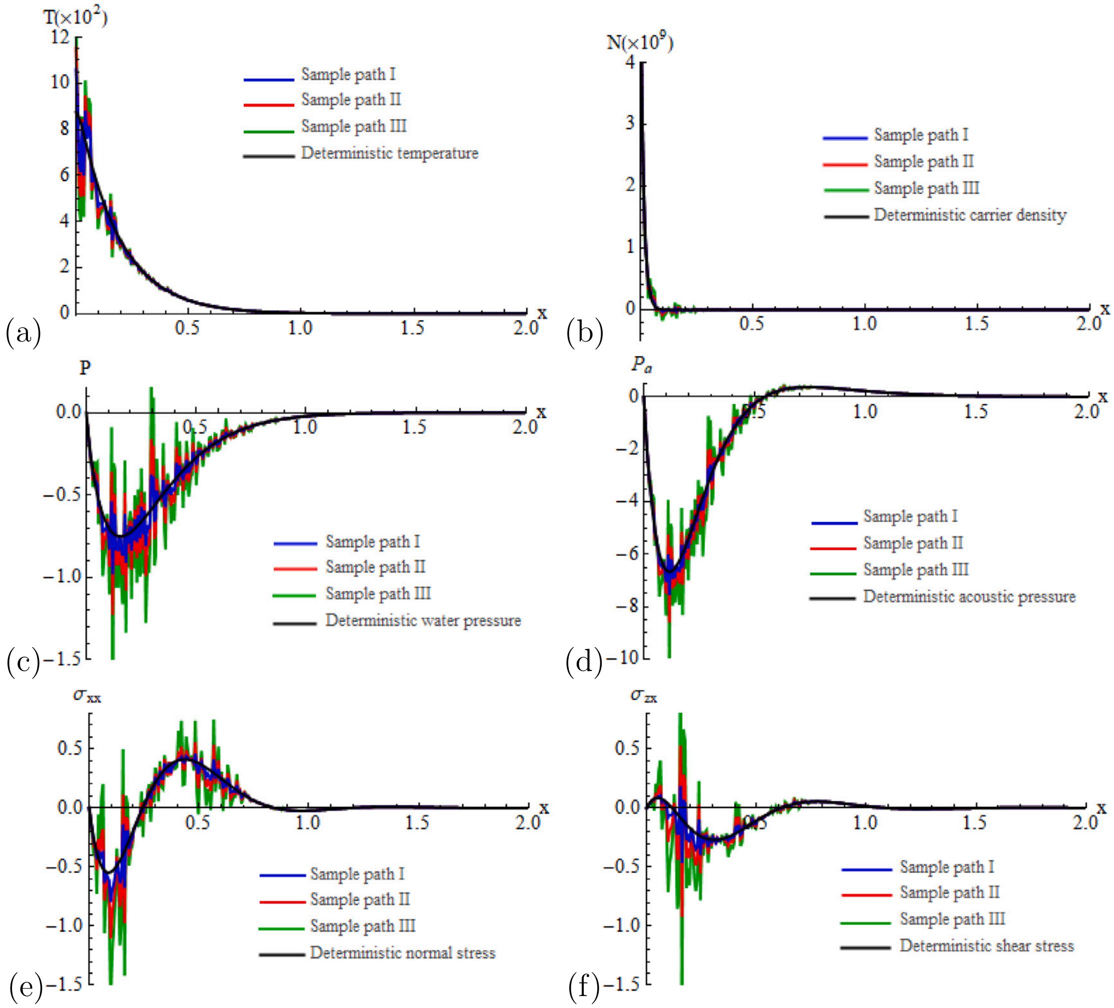

Fig. 6. Distribution of stochastic variables (a) temperature T, (b) carrier density N, (c) water pressure P, (d) acoustic pressure P_a, (e) normal stress σ_{xx}, and (f) shear stress σ_{xz} for different sample paths.

From Fig. 8(a), it is observed that the temperature field is highly localized near the excitation boundary ($x = 0$), confirming that photothermal energy deposition is strongest at the surface. A rapid decay of temperature is observed along the x-direction, indicating strong thermal attenuation and limited penetration depth. Near the boundary, oscillatory variations along the z-direction are evident, reflecting wave-type heat propagation associated with thermal relaxation in the MGN-IV model. As the distance from the boundary increases, the temperature field becomes nearly uniform, demonstrating that the combined effect of small spatial and temporal nonlocal parameters suppresses long-range thermal interactions.

As noticed in Fig. 8(b), the carrier density distribution remains almost spatially uniform throughout the domain, with negligible gradients along both x- and z-directions. This indicates that, under the present deterministic and weakly nonlocal conditions, carrier transport is dominated by diffusion-recombination mechanisms rather than thermoelastic wave effects. The absence of oscillations confirms that the MGN-IV formulation primarily influences thermal and mechanical fields, while the carrier density remains weakly coupled in the deterministic regime.

Fig. 8(c) depicts the pore water pressure exhibiting pronounced spatial variation near the boundary, characterized by alternating compressive and rarefactive regions along the z-direction. These pressure lobes arise due to thermoelastic expansion and contraction of the porous semiconductor matrix. A rapid decay of pressure magnitude along the x-direction indicates attenuation of hydromechanical waves within the medium. Compared to the temperature field, the pore pressure shows stronger sensitivity to thermoelastic coupling, highlighting the significance of poroelastic effects in the MGN-IV framework.

The acoustic pressure distribution in Fig. 8(d) displays strong oscillatory behavior near the excitation surface, confirming efficient generation of acoustic waves under photo-thermoelastic loading. The amplitude of acoustic pressure decreases rapidly with increasing depth, reflecting dissipation due to thermoelastic damping and nonlocal effects. The symmetry of the pressure lobes along the z-direction suggests standing-wave-type behavior governed by boundary conditions and wave interference.

In Fig. 8(e), the normal stress component σ_{xx} exhibits distinct diagonal wave fronts originating from the boundary, indicating directional propagation of thermoelastic stress waves. Alternating tensile and compressive zones are clearly visible, corresponding to elastic wave interference. The stress magnitude decreases significantly along the x-direction, confirming strong mechanical attenuation. The inclined contours reflect coupling between longitudinal and transverse deformation modes, which is enhanced in the MGN-IV model due to thermal relaxation effects.

The shear stress field σ_{xz} also demonstrates diagonal wave-like patterns from Fig. 8(f), though with lower magnitude compared to the normal stress component. High shear stress concentrations are localized near the boundary and decay rapidly into the interior of the medium.

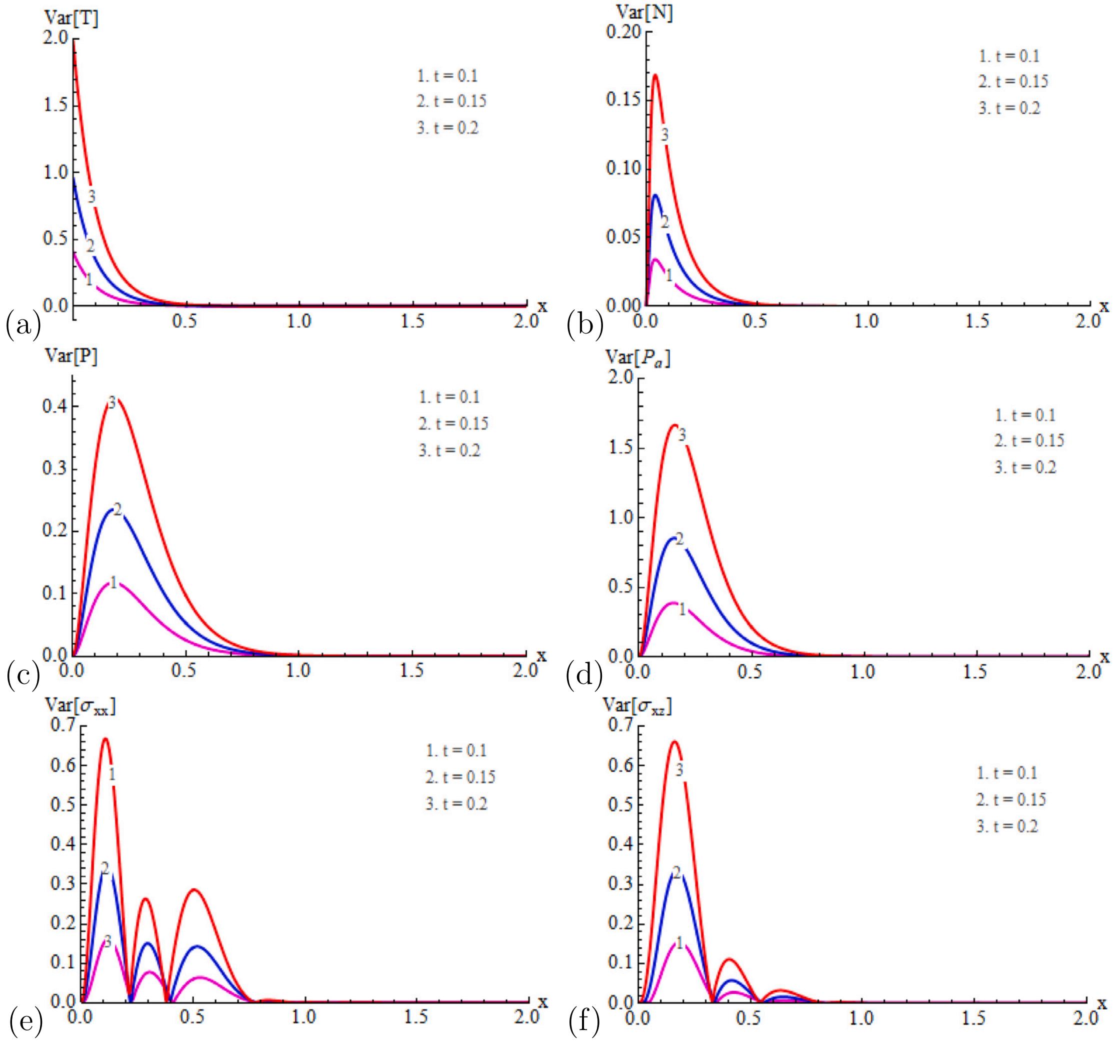

Fig. 7. Distribution of variance of stochastic variables (a) temperature T, (b) carrier density N, (c) water pressure P, (d) acoustic pressure P_a, (e) normal stress σ_{xx}, and (f) shear stress σ_{xz} for different time parameter.

The alternating sign of σ_{xz} indicates shear wave propagation induced by non-uniform thermoelastic deformation. The faster attenuation of shear stress suggests that shear modes are more strongly damped than normal stress modes under spatiotemporal nonlocality.

Overall, these deterministic heat maps reveal that for small spatial and temporal nonlocal parameters, the photo-thermoelastic response of the semiconductor is predominantly localized near the excitation boundary. While thermal, hydromechanical, acoustic, and mechanical fields exhibit strong wave-like behavior with rapid attenuation, the carrier density remains largely unaffected. The MGN-IV model effectively captures the coupled wave phenomena, demonstrating its suitability for analyzing photo-thermoelastic processes in spatiotemporally nonlocal semiconductor media.

8.7. Heat map demonstrating stochastic variables

Figs. 9(a)–9(f) present the heat maps of the stochastic temperature, carrier density, pore water pressure, acoustic pressure, and stress components in a photothermoelastic semiconductor medium for $\ell = 0.01$ and $\tau = 0.01$ under the MGN-IV thermoelastic model. The incorporation of Gaussian white noise through stochastic boundary conditions introduces randomness superimposed on the underlying deterministic wave structure, revealing the sensitivity of coupled physical fields to uncertainty.

The stochastic temperature field (Fig. 9(a)) exhibits strong random fluctuations near the excitation boundary, while these perturbations decay rapidly with increasing depth. This behavior indicates that thermal randomness is primarily boundary-induced and is effectively suppressed by thermal relaxation and spatiotemporal nonlocal effects inherent in the MGN-IV formulation, leading to an exponential decay of temperature variance.

The carrier density distribution (Fig. 9(b)) remains nearly uniform throughout the domain, with only weak stochastic perturbations confined to the vicinity of the boundary. This observation suggests that diffusion and recombination mechanisms smooth out randomness, rendering carrier transport relatively insensitive to stochastic excitation under the present conditions.

In contrast, the pore water pressure (Fig. 9(c)) exhibits pronounced stochastic variability near the boundary, characterized by irregular pressure lobes along the z-direction. The stochastic fluctuations attain a maximum at an intermediate depth before decaying, indicating strong hydromechanical coupling and a peak-type variance behavior under random thermoelastic forcing.

The acoustic pressure field (Fig. 9(d)) shows large stochastic oscillations close to the excitation surface, reflecting the high sensitivity of acoustic waves to boundary randomness. These fluctuations gradually attenuate with depth, and the response approaches the deterministic state due to thermoelastic damping and nonlocal dissipation effects.

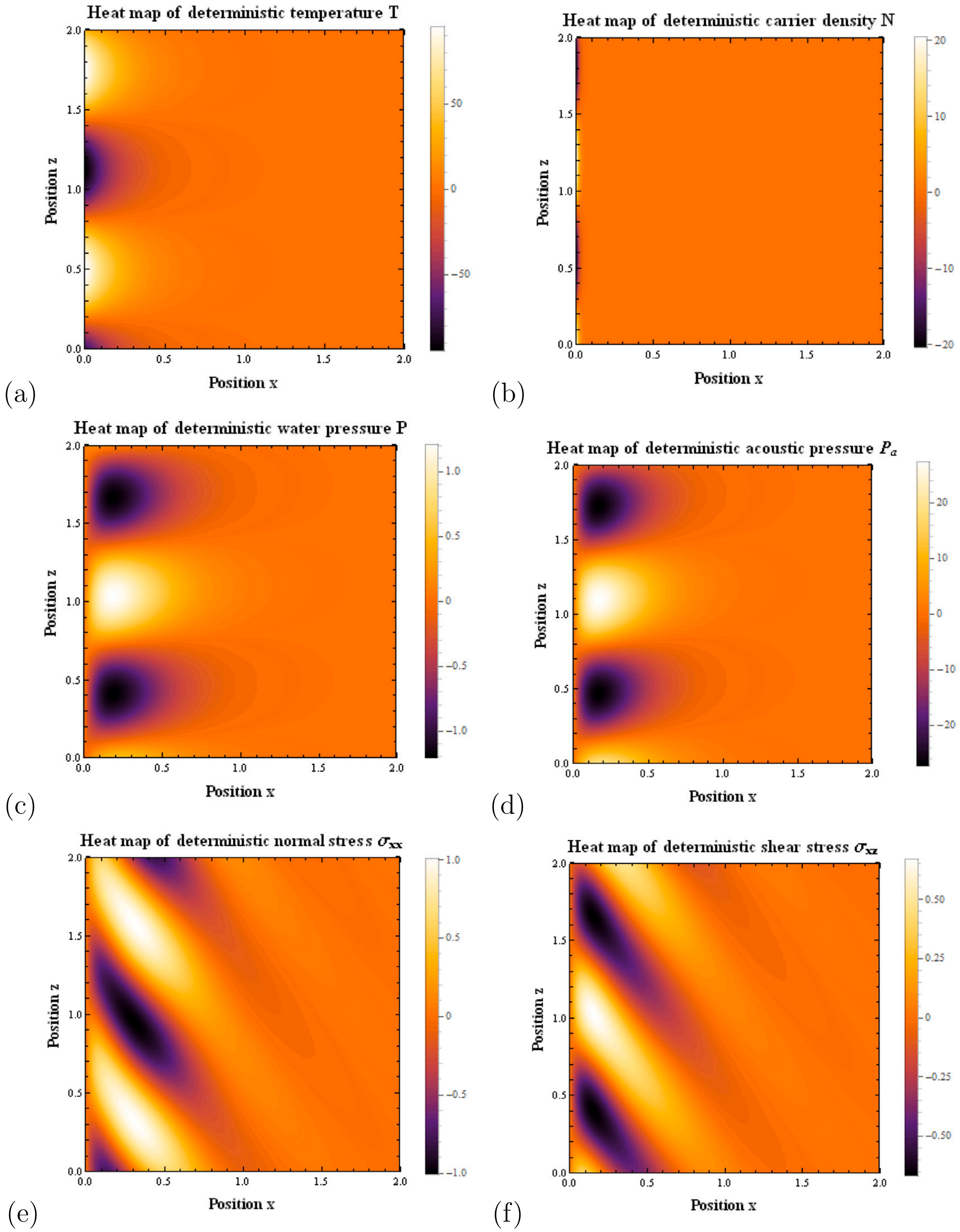

Fig. 8. Heat map of deterministic variables (a) temperature T, (b) carrier density N, (c) water pressure P, (d) acoustic pressure P_a, (e) normal stress σ_{xx}, and (f) shear stress σ_{xz} with respect to dimensionless positions.

The normal stress component σ_{xx} (Fig. 9(e)) displays distorted diagonal wavefronts with localized stochastic stress concentrations near the boundary. The magnitude of stochastic fluctuations decreases with increasing depth, indicating progressive stabilization of the mechanical response. Similarly, the shear stress σ_{xz} (Fig. 9(f)) exhibits strong near-boundary randomness that decays more rapidly than the normal stress, suggesting stronger damping of shear modes under stochastic excitation.

Overall, these results demonstrate that stochastic effects are most significant near the excitation surface and are progressively suppressed within the medium due to spatiotemporal nonlocality and thermal relaxation. While temperature and mechanical fields exhibit variance decay, carrier density remains weakly affected, and pore water pressure, acoustic pressure, and stress fields show peak-type stochastic behavior. These findings highlight the importance of stochastic modeling for

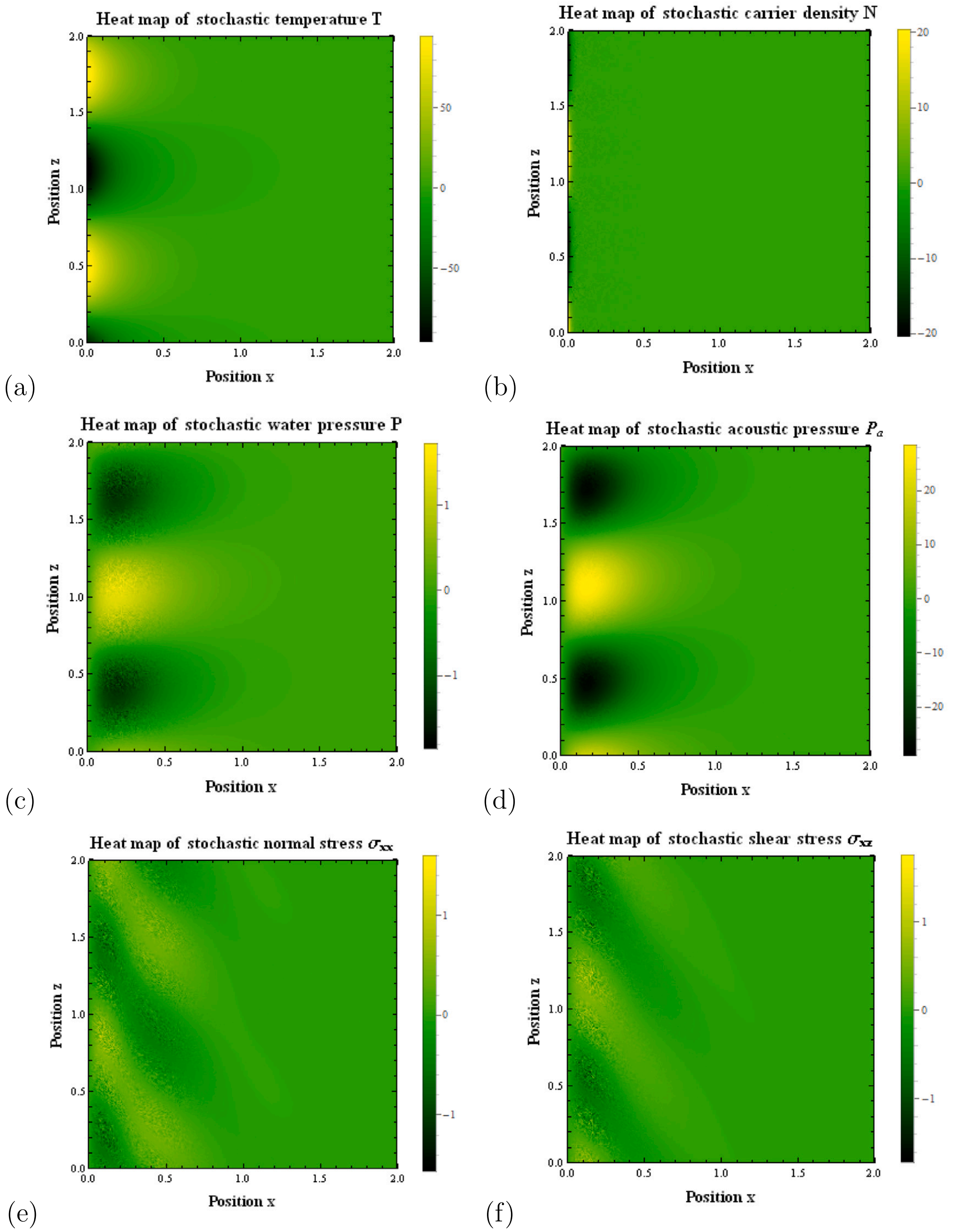
Heat map of stochastic temperature T

Heat map of stochastic carrier density N

Heat map of stochastic water pressure P

Heat map of stochastic acoustic pressure P_a

Heat map of stochastic normal stress σ_{xx}

Heat map of stochastic shear stress σ_{xz}

Fig. 9. Heat map of stochastic variables (a) temperature T, (b) carrier density N, (c) water pressure P, (d) acoustic pressure P_a, (e) normal stress σ_{xx}, and (f) shear stress σ_{xz} with respect to dimensionless positions.

accurately capturing uncertainty in photothermoelastic semiconductor systems.

8.8. Model assessment and validation

The present results are validated against previously established findings, as summarized in Table 2. It has now been numerically validated in Fig. 10 that, in the absence of spatiotemporal nonlocal effects, the computed results of the present problem closely align with those reported in [21], thereby confirming the numerical validity of the formulation.

A detailed graphical comparison between the present model and the results of Alshalhoub et al. [21] is illustrated in Fig. 10 for various thermophysical quantities. From Fig. 10(a), it is observed that the temperature distribution attains its maximum value at the boundary ($x = 0$) and decays rapidly with increasing depth. The present results exhibit excellent agreement with the reference solution, with only negligible deviations near the surface region.

Fig. 10(b) demonstrates the variation of carrier density, which similarly shows a sharp decline from its peak at the boundary and stabilizes as the distance increases. The overlap between the two models confirms the consistency of the carrier transport formulation.

Table 2
Case study of associated models and selected cases.

Case	Condition	Model
I	$\ell = 0,\ \tau = 0,$ $\chi_0 = 1, \quad \chi_1 = 1,$ $\chi_2 = 0, \quad \chi_3 = 1,$ $\chi_4 = 0$	By nullifying certain parameters, case I corresponds to the two-dimensional poro-semiconductor media under Green–Naghdi (GN) theory, which agrees well with the results established by Alshalhoub et al. [21] in the absence of thermal phase-lag parameter.
II	$\tau = 0,$ $\chi_0 = 0, \quad \chi_1 = 1,$ $\chi_2 = 0, \quad \chi_3 = 1,$ $\chi_4 = 1$	By assuming certain values to the parameters, case II justifies the excellent agreement of the present problem with Alshehri et al. [47] in the absence of the effect of variable thermal conductivity in the medium under Lord–Shulman thermoelasticity theory.

In Fig. 10(c), the excess pore water pressure initially exhibits a negative peak near the boundary and gradually approaches zero as x increases. The present results closely follow the trend of the existing model, validating the correctness of the coupled thermo-hydro formulation.

The acoustic pressure profile depicted in Fig. 10(d) reveals a pronounced negative peak near the surface followed by a smooth transition towards equilibrium. The near-perfect agreement between both models highlights the accuracy of the proposed photoacoustic coupling.

Figs. 10(e) and 10(f) illustrate the variations of normal stress σ_{xx} and shear stress σ_{xz}, respectively. Both stress components exhibit oscillatory behavior near the boundary due to strong thermoelastic interactions and gradually diminish with depth. The present model successfully reproduces the amplitude and phase characteristics of the previously reported results, with only minor discrepancies that may be attributed to numerical approximation or modeling assumptions.

Overall, the strong agreement observed across all physical fields confirms that the present formulation is mathematically consistent and physically reliable. This validation establishes the robustness of the proposed model and its capability to accurately recover classical results as limiting cases in the absence of nonlocal and stochastic effects.

9. Concluding remarks

In the present work, a comprehensive theoretical and numerical investigation has been carried out to analyze photo-thermoelastic wave propagation in a porous semiconductor medium incorporating spatiotemporal nonlocal effects and stochastic boundary excitations. The governing equations were formulated within the framework of the modified Green–Naghdi (MGN) thermoelastic theories. The coupled interactions among thermal, electronic, hydromechanical, acoustic, and elastic fields were examined through detailed numerical simulations. The influence of spatial and temporal nonlocal parameters, different thermoelastic models, and stochastic perturbations was systematically explored to elucidate their roles in governing the dynamic response of the medium which have been highlighted in the following concluding remarks.

1. The spatial nonlocal length-scale parameter significantly influences the magnitude and distribution of temperature, water pressure, and stress fields, demonstrating that long-range spatial interactions enhance or attenuate localized thermo-mechanical responses, particularly near the excitation boundary.
2. The temporal nonlocal parameter primarily affects hydromechanical and mechanical fields, leading to attenuation of water pressure and stress magnitudes due to memory-dependent relaxation effects, while leaving temperature, carrier density, and acoustic pressure distributions largely unchanged.
3. A comparative assessment of different modified Green–Naghdi thermoelastic models reveals that generalized MGN theories predict stronger thermoelastic coupling and higher magnitudes of acoustic pressure and stress fields than the conventional Green–Naghdi model, with the MGN-IV model exhibiting the most pronounced responses.
4. The carrier density distribution remains largely insensitive to variations in thermoelastic models and nonlocal parameters, indicating that carrier transport is governed predominantly by diffusion–recombination mechanisms rather than thermoelastic wave effects.
5. The inclusion of stochastic boundary conditions introduces significant randomness in temperature, pressure, and stress fields, particularly near the excitation surface, highlighting the sensitivity of photo-thermoelastic processes to boundary uncertainties.
6. The stochastic variance profiles demonstrate fundamentally different characteristics: thermal and displacement fields exhibit exponentially decreasing variance, while carrier concentration, pore pressure, acoustic pressure, and stress fields display localized maxima at intermediate depths.
7. Heat-map visualizations confirm that thermoelastic, hydromechanical, and acoustic responses are strongly localized near the excited bounding surface and decay rapidly within the medium, while stochastic effects are progressively suppressed by spatiotemporal nonlocality and thermal relaxation.
8. The developed stochastic nonlocal photo-thermoelastic model provides a robust and realistic framework for analyzing coupled multiphysics phenomena in semiconductor materials, offering potential applications in the design and optimization of optoelectronic and photoacoustic devices.
9. **Limitations of the present work:** The analysis is confined to linear thermoelastic behavior, thereby neglecting potential nonlinear effects that could arise under high-intensity laser excitation. Additionally, material properties are considered constant, without accounting for their possible dependence on temperature or other field variables. The stochastic boundary conditions are idealized and based on prescribed statistical characteristics rather than experimentally validated data, which may limit the realism of the model.

10. Future scope of research

Although, the present study is formulated within the framework of linear thermoelasticity, where material properties are assumed to be constant and the governing equations remain linear. This assumption is justified for moderate laser intensities, where temperature rise and carrier excitation remain within ranges that do not significantly alter the intrinsic material parameters.

However, we fully agree that under high-intensity laser excitation, nonlinear effects may become significant. In particular, temperature-dependent material properties (such as thermal conductivity, elastic moduli, and carrier mobility) and nonlinear carrier recombination mechanisms (e.g., Auger recombination or bandgap shrinkage) can influence the system response. These effects may lead to enhanced thermal gradients, modified wave speeds, and amplitude-dependent attenuation, thereby altering both the spatial distribution and temporal evolution of the thermophysical fields (see Fig. 11).

From a physical standpoint, the inclusion of such nonlinearities would likely result in stronger localization of temperature near the excitation boundary, deviations from the exponential decay profiles observed in the linear model, and possible distortion of wavefronts in acoustic and stress fields. Additionally, nonlinear recombination processes could significantly modify the carrier density distribution, particularly in regions of high excitation, thereby influencing the coupled thermoelastic response. Such extension of the present framework will

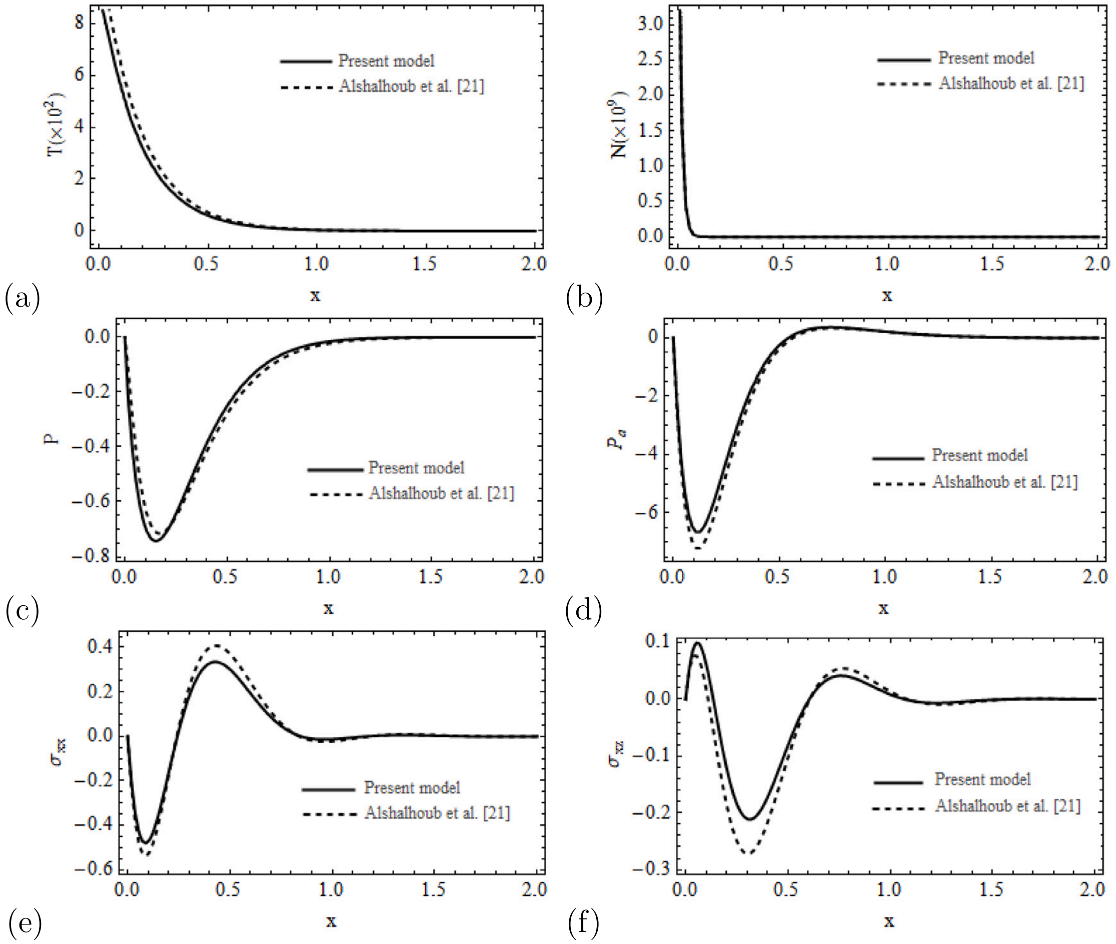

Fig. 10. Comparative study of deterministic variables (a) temperature T, (b) carrier density N, (c) water pressure P, (d) acoustic pressure P_a, (e) normal stress σ_{xx}, and (f) shear stress σ_{xz} with respect to position x between the computed results of present model and the estimated results of Alshalhoub et al. [21].

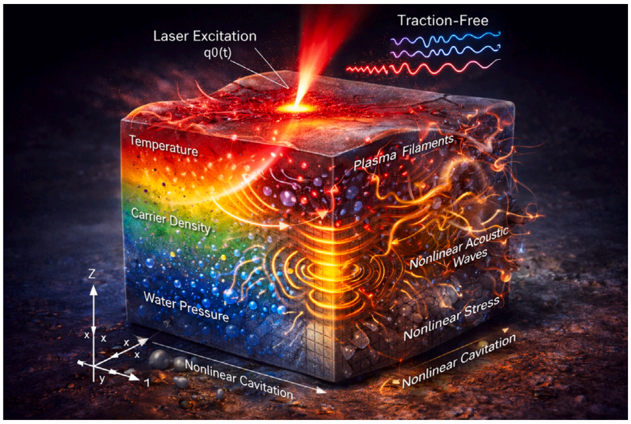

Fig. 11. Schematic diagram describing nonlinear effects.

provide a more comprehensive description, particularly for high-power laser applications.

CRediT authorship contribution statement

Abhik Sur: Supervision, Methodology. **Marin Marin:** Writing – review & editing, Validation, Software. **Argha Nath Bhattacharyya:** Visualization, Methodology. **Murat Yaylacı:** Software, Conceptualization. **Soumik Das:** Writing – original draft, Investigation.

Declaration of Generative AI and AI-assisted technologies in the writing process

This statement confirms that the authors did not use AI in the core process

Funding

No external funding received regarding this research.

Declaration of competing interest

The authors declare that they have no known competing financial interests or personal relationships that could have appeared to influence the work reported in this paper.

Acknowledgments

Authors are also sincerely thankful to Amrita Vishwa Vidyapeetham, Mysuru campus, India, Sister Nivedita University, India, Transilvania University of Brasov, Romania, and Recep Tayyip Erdogan University, Turkey for supporting immensely by providing great opportunity, guidance, best facilities and equipments.

Data availability

All data generated or analyzed during this study are included in this published article.

References

[1] Hoel PG, Port SC, Stone CJ. Introduction to stochastic processes. Waveland Press; 1986.

[2] Sherief HH, El-Maghraby NM, Allam AA. Stochastic thermal shock problem in generalized thermoelasticity. Appl Math Model 2013;37(3):762–75.

[3] Miyata H, Iijima S, Ooshima R, Abe T, Hisamatsu T, Hamamatsu T. Application technology on ceramics for structural components of high-temperature machines. JSME Int J Ser 1, Solid Mech Strength Mater 1989;32(4):596–604.

[4] Mori M, Kondo M. Temperature and thermal stress analysis in a structure with uncertain heat transfer boundary conditions. Trans Jpn Soc Mech Eng A 1993;59:1514–8.

[5] Shimakawa T, Take K, Uno M, Takamatsu S, Takahashi Y, Miura N. Development of the evaluation method for crack propagation due to thermal striping. Nucl Eng Des 1992;138(3):283–96.

[6] Meghana A, Dutta R, Gupta V, Das S, Singhal A, Sur A, Almohsen B. Shear waves induced vibration in a size-dependent loosely-bonded viscoelastic–flexoelectric material structure subjected to fractional derivative. Eur J Mech A Solids 2025;112:105666.

[7] Sur A. Memory response on wave propagation in a micropolar magneto-thermo-viscoelastic half-space. Waves Random Complex Media 2022;32(3):1468–96.

[8] Marin M. Some basic theorems in elastostatics of micropolar materials with voids. J Comput Appl Math 1996;70(1):115–26.

[9] Marin MI, Agarwal RP, Abbas IA. Effect of intrinsic rotations, microstructural expansion and contractions in initial boundary value problem of thermoelastic bodies. Bound Value Probl 2014;2014(1):129.

[10] Zeeshan A, Khan MI, Ellahi R, Marin M. Computational intelligence approach for optimising mhd casson ternary hybrid nanofluid over the shrinking sheet with the effects of radiation. Appl Sci 2023;13(17):9510.

[11] Song H, Qing H. Static extension and vibration analysis of piezoelectric semiconductor nanobars based on two-phase local/nonlocal integral models. Acta Mech 2026;237(1):299–315.

[12] Song H, Li C, Qing H. Size-dependent bending and buckling analysis of piezoelectric semiconductor nanobeam based on two-phase local/nonlocal integral models: H. Song et al. Int J Mech Mater Des 2026;22(1):48.

[13] Larbi L Ould, Saad M, Zouatnia N, Hadji L, Sayyad AS. A simple refined plate theory for buckling problems of in-plane bi-directional functionally graded plates with porosity under various boundary conditions. Mech Adv Mater Struct 2025;32(3):403–12.

[14] Djebbour K Djilali, Mokhtar N, Hassen AA, Alghanmi RA, Hadji L, Riadh B. An enhanced quasi-3D HSDT for free vibration analysis of porous FG-CNT beams on a new concept of orthotropic VE-foundations. Mech Adv Mater Struct 2025;32(5):893–909.

[15] Nebab M, Dahmane M, Belqassim A, Atmane HA, Bernard F, Benadouda M, Bennai R, Hadji L. Fundamental frequencies of cracked FGM beams with influence of porosity and Winkler/Pasternak/Kerr foundation support using a new quasi-3D HSDT. Mech Adv Mater Struct 2024;31(28):10639–51.

[16] Hadji L, Plevris V, Madan R. Dynamic behavior of imperfect FGM beams with various porosity distribution rates: analysis and modeling. In: The International Conference on Net-Zero Civil Infrastructures: Innovations in Materials, Structures, and Management Practices. Springer; 2024, p. 1515–27.

[17] Lotfy K, El-Bary A, Elidy E, Tantawi R, Ahmed A, Mohamed MS, Mahdy A. A novel model of stochastic photo-elasto-thermodiffusion waves interaction in semiconductors. Mech Solids 2024;59(4):2301–21.

[18] Sherief HH, El-Maghraby NM, Allam AA. Stochastic thermal shock problem in generalized thermoelasticity. Appl Math Model 2013;37(3):762–75.

[19] Allam AA. A stochastic half-space problem in the theory of generalized thermoelastic diffusion including heat source. Appl Math Model 2014;38(21–22):4995–5021.

[20] Kant S, Mukhopadhyay S. Investigation of a problem of an elastic half space subjected to stochastic temperature distribution at the boundary. Appl Math Model 2017;46:492–518.

[21] Alshalhoub S, Nasr MAbou El, Lotfy K, Elshazly IS, El-Bary AA, Tantawi R, Ahmed A. A stochastic photoacoustic thermo-hydro-mechanical photoelastic wave propagation investigation in poro-semiconductors materials. Int Commun Heat Mass Transfer 2025;169:109951.

[22] Yu Y-J, Wu H, Deng Z-C. New insights on fractional thermoelasticity from anomalous heat conduction. Acta Mech Sin 2024;40(5):423419.

[23] Huang Y, Yan L, Wu H, Yu Y. New insights on generalized heat conduction and thermoelastic coupling models. Appl Math Mech 2025;46(8):1533–50.

[24] Sur A, Lotfy K, Yaylacı M, Das S. Mesoscale damping and stiffening in silicon microbeams: A heat-map study using a memory-dependent Green–Naghdi model. Int Commun Heat Mass Transfer 2026;173:110742.

[25] Meghana A, Marin M, Dutta R, Gupta V, Sur A, Yaylacı M, Das S. Dynamic response of a loosely bonded viscoelastic/porous piezoelectric bilayer microplate to a frictional moving load over a parabolic discontinuity. Appl Math Model 2026;116904.

[26] Sur A, Dutta R, Yaylacı M, Das S. Thermo-diffusive response of fractal spherical tumors under modified Green–Naghdi heat conduction models. J Therm Biol 2026;104440.

[27] Lotfy K, Ahmed A, El-Bary A, El-Shekhipy A, Tantawi RS. A novel stochastic photo-thermoelasticity model according to a diffusion interaction processes of excited semiconductor medium. Eur Phys J Plus 2022;137(8):972.

[28] Lotfy K, Ahmed A, El-Bary A, Tantawi RS. A novel stochastic model of the photo-thermoelasticity theory of the non-local excited semiconductor medium. Silicon 2023;15(1):437–50.

[29] Mandelis A, Nestoros M, Christofides C. Thermoelectronic-wave coupling in laser photothermal theory of semiconductors at elevated temperatures. Opt Eng, Bellingham 1997;36(2):459–68.

[30] Sharma A, Sharma J, Sharma Y. Modelling reflection and transmission of acoustic waves at a semiconductor: fluid interface. Adv Acoust Vib 2012;2012(1):637912.

[31] Sell J. Photothermal investigations of solids and fluids. Elsevier; 2012.

[32] Sur A. Photo-thermoelastic inter action in a semiconductor with cylindrical cavity due to memory-effect. Mech Time-Dependent Mater 2024;28(3):1219–43.

[33] Sur A. Photothermoelastic interaction in a two-dimensional semiconductor with nonlocal stress theory. Int J Comput Methods Eng Sci Mech 2024;25(4):248–64.

[34] Sur A, Lotfy K, Ranjit NK, Das S. Advanced finite element analysis of photothermal response in cylindrical semiconductor with spatial nonlocality and memory-dependent heat transport. Int Commun Heat Mass Transfer 2025;169:109771.

[35] Lotfy K, Sharma S, Halouani B, Ahmed A, El-Bary AA, Tantawi RS, Elidy ES. Stochastic process of magneto-photo-thermoelastic waves in semiconductor materials with the change in electrical conductivity. J Elasticity 2025;157(1):11.

[36] Taha HH, Ahmed A, El-Bary AA, Tantawi R, Lotfy K, Fawzy MA. White noise effects on stochastic thermo-hydro-mechanical photoelastic interactions in poro-semiconductors. J Low Freq Noise, Vib Act Control 2025;14613484251347811.

[37] Tam AC. Applications of photoacoustic sensing techniques. Rev Modern Phys 1986;58:381–431. http://dx.doi.org/10.1103/RevModPhys.58.381, https://link.aps.org/doi/10.1103/RevModPhys.58.381.

[38] Sell J. Photothermal investigations of solids and fluids. Elsevier; 2012.

[39] Todorović D, Nikolić P, Bojičić A. Photoacoustic frequency transmission technique: electronic deformation mechanism in semiconductors. J Appl Phys 1999;85(11):7716–26.

[40] Alenazi A, Ahmed A, El-Bary AA, Tantawi RS, Lotfy K. Moisture photo-thermoelasticity diffusivity in semiconductor materials: a novel stochastic model. Crystals 2022;13(1):42.

[41] Green AE, Lindsay K. Thermoelasticity. J Elasticity 1972;2(1):1–7.

[42] Sherief HH, El-Maghraby NM, Allam AA. Stochastic thermal shock problem and study of wave propagation in the theory of generalized thermoelastic diffusion. Math Mech Solids 2017;22(9):1767–89.

[43] Ntziachristos V. Going deeper than microscopy: the optical imaging frontier in biology. Nature Methods 2010;7(8):603–14.

[44] Lotfy K, El-Sapa S, Ahmed A, El-Bary AA, Tantawi RS, Ahmed MH, Elidy ES. Stochastic wave propagation in magneto-thermoelastic materials subjected to the change in electrical and thermal conductivity. AIP Adv 2024;14(1).

[45] Li Y, Su C. Stochastic evolution mechanism in random thermoelastic vibration captured using the explicit time-domain method. Int J Mech Sci 2021;205:106616.

[46] Lotfy K, Elshazly IS, Halouani B, Sharma S, El-Bary AA, Hassanin W. Nonlocal photoacoustic waves in hydro-poroelastic semiconductors with variable thermal conductivity subjected to mass diffusion. Int Commun Heat Mass Transfer 2025;163:108692.

[47] Alshehri HM, Lotfy K, Raddadi MH, El-Bary AA. A nonlocal photoacoustic effect with variable thermal conductivity of semiconductor material subjected to laser heat source. Results Phys 2024;61:107715.